Rational Improvement of the Activity of a Nitrite Reductase Model

A THESIS
SUBMITTED TO THE FACULTY OF THE GRADUATE SCHOOL
OF THE UNIVERSITY OF MINNESOTA
BY

Jacob Nicholas Strange

IN PARTIAL FULFILLMENT OF THE REQUIREMENTS
FOR THE DEGREE OF
MASTER OF SCIENCE

Steven M. Berry

May 2014

Acknowledgements

I would fisrt like to thank my parents and family for support throughout my education. I would also like to thank Dr. Berry for his instruction and advisement through these last years. Also, I am very grateful to all of my fellow graduate students and professors at UMD for the experiences, education and friendships which I have gained. Specifically graduate students Garrett Stoddard and Balabhadra Khatiwada as well as undergraduate students Paul Yager and Christine Hedstrom.

Abstract

Nitrite reductase (NiR) is a bacterial enzyme that catalyzes the one electron reduction of nitrite (NO_2^-) to nitric oxide (NO). Through site-directed PCR mutagenesis, variants of the electron transfer protein azurin (See figure) were rationally designed to mimic Nitrite Reductase (NiR) in an attempt to increase our knowledge about enzyme function and design. Several variants were created by incorporation of a Type 2 copper center on the surface of the protein. Further mutations were added to aid in electron transfer as well as to match the potential of the Type 1 copper in azurin to that of the Type 1 copper in NiR. Each variant was characterized using EPR, UV-Vis and mass spectroscopy. Finally, we characterized each variant using Michaelis-Menten kinetics. This activity was determined using the Griess assay, which allows us to spectrophotometrically quantify the amount of nitrite in our reaction. We compared the activity of our NiR models. The results show that the variant designed for faster electron transfer did not increase the activity of our enzyme, but did increase activity when added with the other mutations. The two variants designed to decrease the reduction potential of the Type 1 copper site were found to increase the activity by themselves, but decrease the activity when combined.

Table of Contents

List of Tables

List of Figures

Chapter 1: Introduction

1.1 Nitrite Reductase and its Role in the Nitrogen Cycle:

Nitrogen is the fifth most plentiful element in our solar system and comprises approximately 78% of Earth's atmosphere.[1] Nitrogen is essential for life on Earth and is most commonly found in the form of N_2.[1] N_2 is an inert form of nitrogen that must be converted into ammonia, NH_3, or nitrate, NO_3^-, before it can be utilized by biological organisms.[1] Because of the abundance of the inert form of nitrogen, as well as the requirement that it be converted before use in biological systems, nitrogen availability often limits the productivity of many ecosystems and can thus have an impact on the carbon cycle as well.[2] The process of reducing N_2 into ammonia is known as nitrogen fixation and is achieved by prokaryotes as well as some eukaryotes working in a symbiotic relationship with prokaryotes.[1] N_2 can also be converted into ammonia and nitrate during lightning storms, however this process contributes less than 10% of what is produced by biological systems.[2] Along with being a necessary part for healthy ecosystems, biologically available nitrogen can also sometimes have negative impacts. Nitrates have the ability to leech through the ground into water sources, altering fresh and salt water ecosystems, depleting minerals and acidifying soils.[2] Reactive oxides of nitrogen also have the capability of contributing to acid rain by the formation of nitric acid when released as gasses.[2]

In biological systems, the reduction of one molecule of nitrogen gas into two molecules of ammonia is an 8 electron process that requires 16 ATP's and is only known to be achieved by one enzyme, nitrogenase. Although nitrogenase is common among prokaryotes, most organisms obtain ammonia either directly or via the reduction of

nitrates to ammonia by either dissimilatory nitrate reduction or through denitrification and then nitrogen fixation (see Figure 1). The main focus of the research presented in this thesis was on a mimic of an enzyme found in the pathway of denitrification. Specifically the enzyme catalyzing the step in denitrification where nitrite (NO_2^-) is reduced to nitric oxide (NO), known as nitrite reductase (See Figure 1).

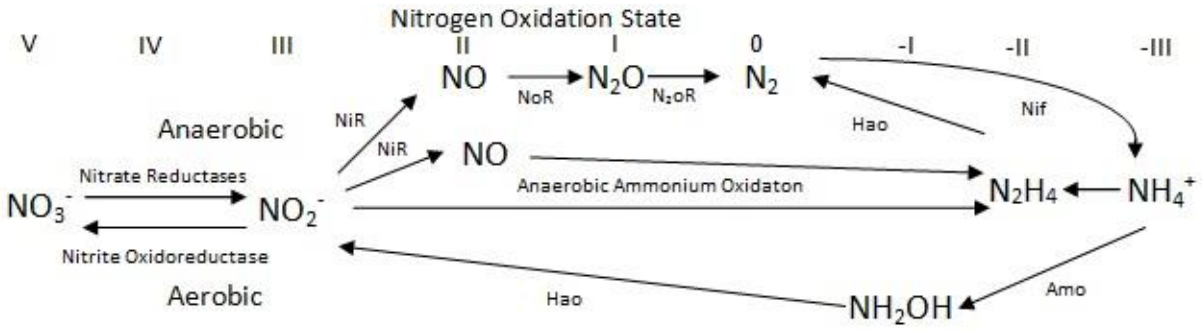

Figure 1 - Major biological nitrogen pathways as well as the enzymes associated with each step. NiR – nitrite reductase, NoR – nitrous oxide reductase, Hao – hydroxylamine monooxygenase, Amo – ammonium monooxygenase, Nif – nitrogenase. (Adapted from Canfield[1])

Figure 2 – The steps of the denitrification pathway.

Nitrite reductases (NiR) are a family of enzymes with two broad classes: one catalyzes the reduction of nitrite through an iron heme site, and the other is a copper protein with two types of copper sites that give rise to it its function. Both enzymes

catalyze the reduction of nitrite to nitric oxide, a one electron step in the denitrification pathway.[3] The focus of the work in this thesis was to model the structure and function of the latter, copper NiR. To model NiR it was important to identify factors that are believed to be important for copper nitrite reductase function.

The first factors that are important for function are the presence of two copper sites and the types of each copper (see Figure 3).

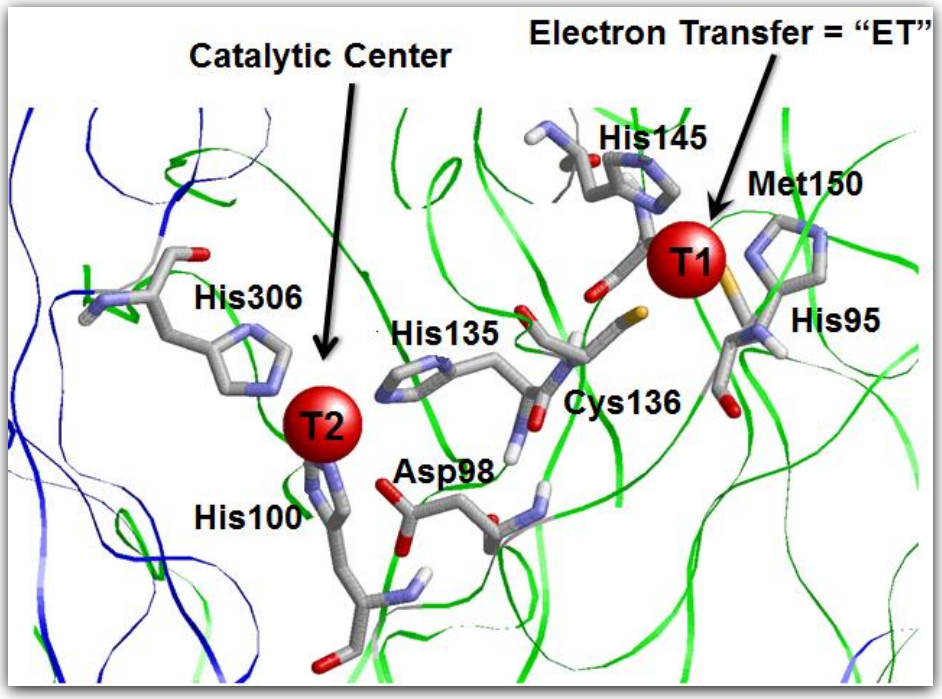

Figure 3 – The Type 1 and Type 2 copper sites of nitrite reductase from *Alcaligenes faecalis* PDB Id: 1AS7.

The first copper site is identified as a copper Type 1 electron transfer site. These sites are well known to have a greatly conserved structure of two nitrogen bonds from histidines as well as a highly covalent copper sulfur bond to a cysteine and a weakly

bound axial methionine.[3-7] These sites are found in a wide range of copper proteins and give rise to a characteristic blue or green color due to the large intensity of a ligand to metal charge transfer from the cysteine to the copper.[8] This gives rise to two further subclasses of NiRs, those called blue NiR and green NiRs that differ in the nature of their Type I copper center. Blue Type 1 copper sites get their color from an approximately 600 nm absorption band which arises from a S(Cys) pπ → Cu $3d_{x^2-y^2}$ transition.[6,8] The Type 1 copper sites found in green nitrite reductases have a slightly different geometry around the copper, giving rise to a S(cys) pσ → Cu $3d_{x^2-y^2}$ transition with an increased absorption around 450 nm.[6,8] The absorption is due to the strong covalent cysteine ligand as confirmed by Mizoguchi in 1992 when the Type 1 site in azurin, which is similar in structure to the Type 1 site in NiR, had the cysteine mutated into an aspartic acid, which eliminated the absorption band at 600 nm.[9]

Another distinct characteristic of Type 1 copper sites is their wide range of redox potentials and their electron transfer ability. The Type 1 copper center potential in NiR was measured around 255 mV, which is on the lower end of the Type 1 reduction potential spectrum, with values ranging from 184 mV in a stellacyanin up to 1000 mV in human ceruloplasmin.[10-12] A d^{10} copper, or Cu(I), has a preferred tetragonal geometry and prefers soft/soft interactions such as sulfur binding while d^9 coppers, or Cu(II) prefer a square planar geometry and more hard/hard interactions like binding nitrogen.[8] The Type 1 sites in NiR and other blue copper proteins have more of a mix of the two ligands with a distorted tetrahedral geometry that does not change when the protein is either in the oxidized or reduced form. This lack of reorganization upon changing of oxidation

states is one of the factors that give rise to the redox potentials of T1 copper sites, as well as their ability to quickly transfer electrons.[8,13]

The next important aspect in the function of NiR is the second copper site present, designated as the Type 2 copper. The Type 2 copper site is the catalytic center and is where nitrite is reduced. They consist of a copper bound by 3 histidines and a solvent molecule, usually water when substrate is not present, in a distorted tetrahedral geometry.[3,6,14] In the presence of substrate, the water is displaced and nitrite binds. Although the products of nitrite reduction are known, the exact order of the mechanism is still unclear. One proposed mechanism for reduction is proposed by Adman (See Figure 4).[16] In this mechanism, nitrite first binds to the oxidized copper ion. The oxidized copper ion is then reduced by an electron that is transferred from the pre-reduced Type 1 copper site. This electron, as well as a proton from a neighboring aspartic acid, is then used to reduce nitrite and form nitric oxide as well as a hydroxide ion. The nitric oxide then dissociates and the hydroxide is protonated, returning water to the Type 2 copper sites before the process is repeated again.[15]

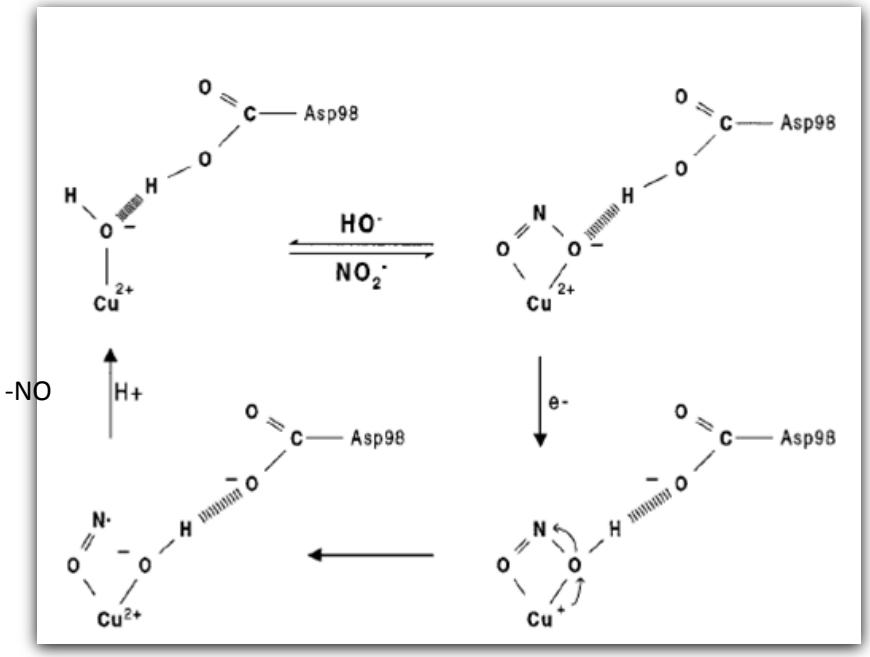

Figure 4 – Proposed mechanism for the reduction of nitrite to nitric oxide.[16]

The above mechanism is supported by Pinho as well as Strange, who both have shown through EPR, ligand binding studies and X-ray crystals that nitrite preferentially binds to the oxidized Type 2 copper sites before electron transfer from the type one copper sites occur.[6,17] There has been a second mechanism proposed, such as the work done by Wijma, where nitrite binding occurs after the reduction of the type two copper sites during conditions with low nitrite concentrations and that the mechanism switches to binding to the oxidized copper first when higher nitrite concentrations are seen.[3,18]

The last property of nitrite reductase that is thought to be important for function is the peptide backbone that connects the cysteine of the Type 1 copper site to one of the histidines of the Type 2 copper site. This peptide bond can be seen above in Figure 3 between Cys136 and His 135 in NiR from *Alcaligenes faecalis*. This peptide bond is proposed to be the pathway which the electron takes when transferred from the type one

copper site to the Type 2 copper site.[19] This is predominantly supported by the delocalization of the electron on the oxidized type one copper site on the cysteine which gives NiR its intense blue or green color, depending on the NiR subtype.[19]

NiRs are efficient enzymes at producing NO from nitrite. Turnover numbers for native NiR's range from 0.62 s^{-1} for NiR from *Pseudomonas chlororaphis* at a pH of 7.0 up to 1478 s^{-1} for NiR from *Alcaligenes faecalis* at a pH of 6.0.[3,6] The activity for NiR is pH dependent, as can be seen in Figure 5 below, with typical results of faster rates at lower pH since the reduction of nitrite to nitric oxide requires a proton (see Reaction 1).[14]

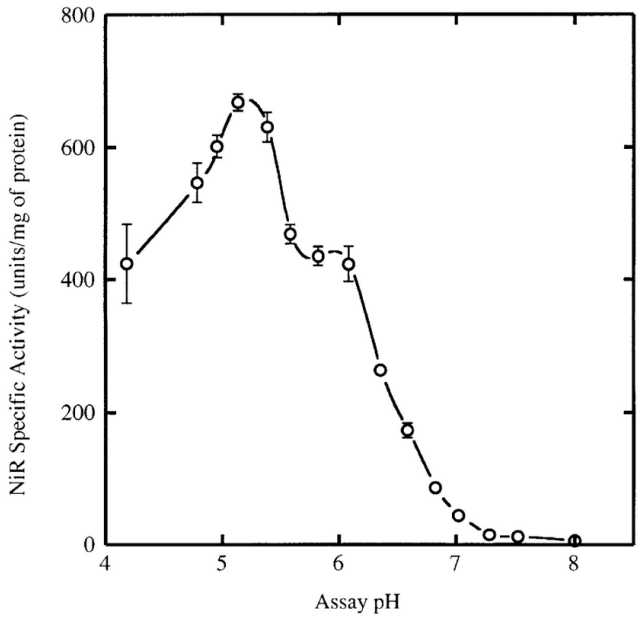

Figure 5 - The pH dependence of NiR from *Alcaligenes xylosoxidans.*[14]

$$NO_2^- + 2\,H^+ + e^- \leftrightarrow NO + H_2O \quad (1)$$

1.2 Using Azurin as a Model for Nitrite Reductase:

Azurin is a copper protein containing a single type one copper site, and it is the scaffolding we mutated to make models that mimic the activity of nitrite reductase. Azurin is found in the periplasm of a range of bacteria and has been shown in vitro to be a redox partner of nitrite reductase. [20-23] Type 1 copper sites, like the one found in azurin and NiR, are often involved in respiration and facilitate electron transfer between catalytic sites and other electron donors.[24] Azurin is 14 kDa in size and consists of 128 amino acids arranged in a β-barrel structure which is configured in a double wound Greek key topology with two beta sheets and a 13 residue long alpha helix.[25,26]

In addition to the role of azurin in the electron transfer pathway, it has also been shown *in vitro* to interact with p53, a tumor suppressor found in multicellular organisms.[27,28] In these cases, azurin has been found to have the ability to enter cancer cells and form complexes with p53. This then raises p53 levels within the cell and leads to an increase in the production of reactive oxygen species which in turn induce apoptosis of the cell.[27,28]

Our modeling of the native NiR's activity was achieved by making various mutations to this blue copper protein azurin. Azurin already has a Type 1 copper center that consists of two histidines, a methionine and a cysteine, as well as a weak interaction with the carbonyl from a nearby glycine forming a pseudo trigonal bipyramidal geometry.[7,29] This Type 1 copper is comparable to the Type 1 copper center in NiR's, having a similar geometry, UV-Vis spectra and also comparable EPR parameters (see Tables 4-7 within the EPR results). There are a few differences between azurin and

native NiR, however, one being the reduction potential of the Type 1 copper. The redox potential of NiR's Type 1 copper site is about 250 mV, whereas the redox potential of the Type 1 copper in azurin is around 357 mV.[6,7,10,12,24,30] Another difference between azurin and NiR is the lack of a Type 2 copper site in azurin, which must be added to the surface of the protein. Both of these differences give us an opportunity to rationally design mutations into azurin which we hypothesize to result in comparable nitrite reductase activity of the two enzymes.

1.3 The Parent Azurin-NiR Variants:

There were four "parent" variants that were previously created to take care of one of the factors that would make the azurin model mimic NiR.[8] This was the incorporation of a second copper binding site on the surface of azurin, with the four designed variants named PHM, PHM3His, NiR and NiR3His. The Type 2 copper sites in PHM and PHM3His were originally designed to structurally mimic the copper M sites of peptidyl α-hydroxylating monooxygenase, but since they resemble the Type 2 site in native NiR they were also tested for their activity in reducing nitrite. The models NiR and NiR3His were designed to specifically recreate the Type 2 site found in native NiR.

The PHM Type 2 copper site was designed by incorporating a methionine on one strand and two histidines on an adjacent strand, both of which were located on the surface of the protein and approximately 12 Å from the Type 1 copper site. The mutations that achieved this were Gln8Met, Gln14His, and Asn16His. The PHM3His variant was designed using the same mutation sites, except Gln8 was mutated to a histidine instead of a methionine. The NiR and NiR3His variants were designed in a similar fashion, with

NiR having a histidine incorporated into one strand and an aspartic acid and histidine on a neighboring strand in the same area of the protein as the PHM variants. The specific mutations were Asn10His, Gln14Asp and Asn16His. NiR3His used the same mutation sites with the difference being a Gln14His mutation instead of the Gln14Asp.[31] An example of one of the incorporated Type 2 sites, in NiR3His azurin is shown in Figure 6.

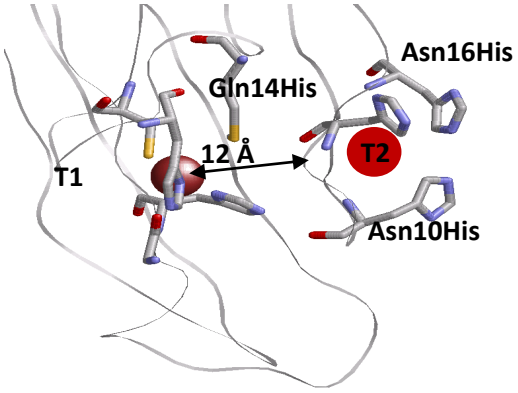

Figure 6 – The Type 2 copper site as designed for NiR3His. This is the same relative position of the Type 2 site for all four of the parent variants.

1.4 The Three Variants of Parent Mutant NiR3His azurin: The "Second Generation" Variants

As is discussed in Chapter 3, the activity of these variants was measured. The most active variant was NiR3His. In order to further increase the nitrite reductase activity of this and our other models, there were three residues which were selected for a "second generation" of mutations. These sites were Phe114, Met121 and Phe15. The

positions of each of those relative to the Type 1 copper site and the designed Type 2 site are shown below in Figure 7.

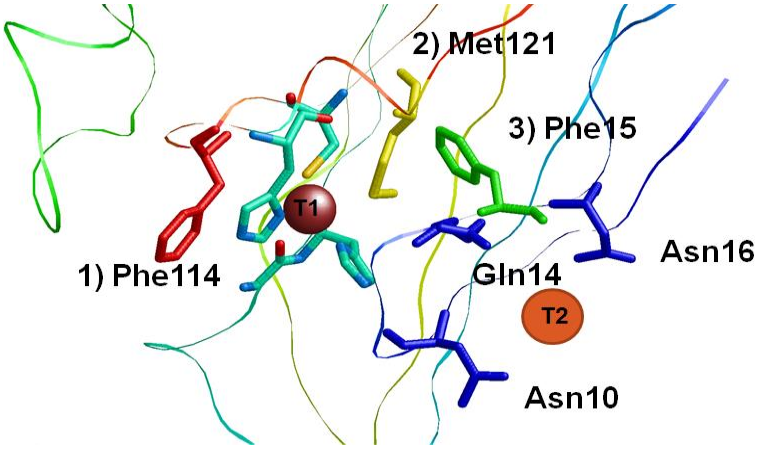

Figure 7 – The positions of the three residues that were mutated in the 2nd generation variants (red, yellow and green) shown in relation to the Type 2 copper (blue residues) site for NiR/NiR3His.

In addition to adding a second copper, there was also the need to lower the redox potential of the Type 1 copper center in azurin from approximately 360 mV to 250 mV in order to match that of the Type 1 copper in native NiR. There were two ways that this was achieved; the first was the mutation of the residue Phe114 to a proline. This mutation eliminates a hydrogen bond between Phe114 and Cys112 which then allows Cys112 to move closer to the Type 1 copper increasing electron density (shown in Figure 8).[7] When Cys112 is closer to the type 1 site it increases the electron density on the copper and reduces the reduction potential by about 100 mV.[7]

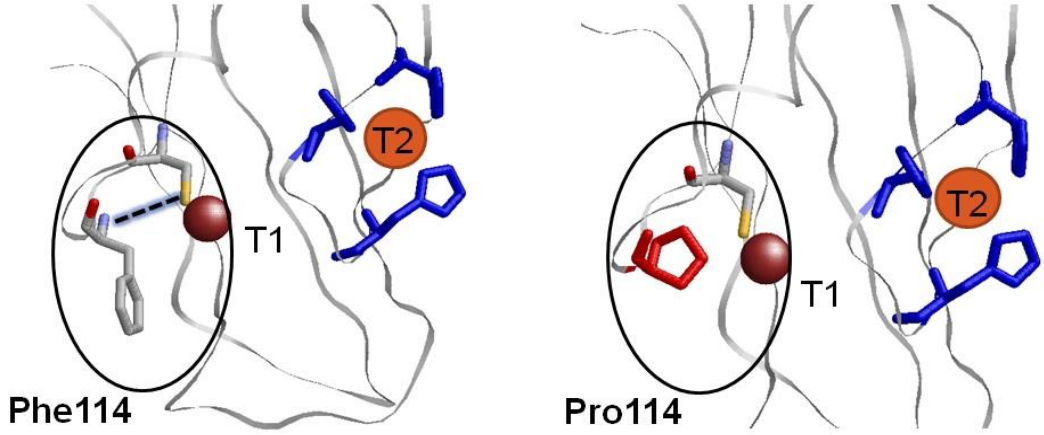

Figure 8 – The mutation of Phe114 into Pro114 for the NiR3His model.

A second way that the redox potential of our models was adjusted was with the Met121Gln variant which was designed to lower the potential of the Type 1 copper center in azurin by about 100 mV.[7] This mutation changes the axial ligand Met121 to a glutamine and, similar to the Phe114Pro mutation, has the effect of disrupting a hydrogen bond between Phe114 and Cys112.[7]

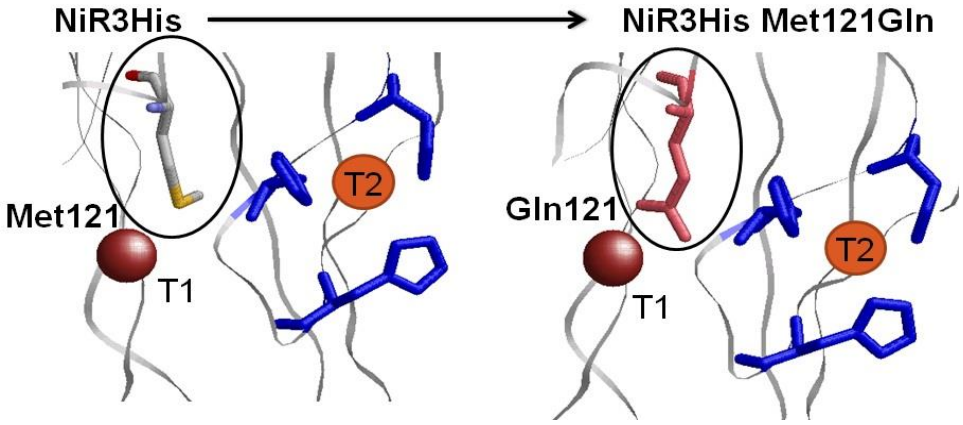

Figure 9 – The mutation of M121 into Gln121 for the NiR3His model.

The third and final "second generation" variant was designed to aid in the transfer of an electron between the type 1 copper and the type 2 copper, similar to what the peptide bond between His135 and Cys136 accomplishes for native NiR, shown in Figure 10. To do this, Phe15 was replaced with a tryptophan due to the known ability of tryptophan to aid in long range electron transfer.[32] Similar work was done by Gray who showed a tryptophan residue can help facilitate and speed the transfer of an electron at distances of over 20 Å.[32]

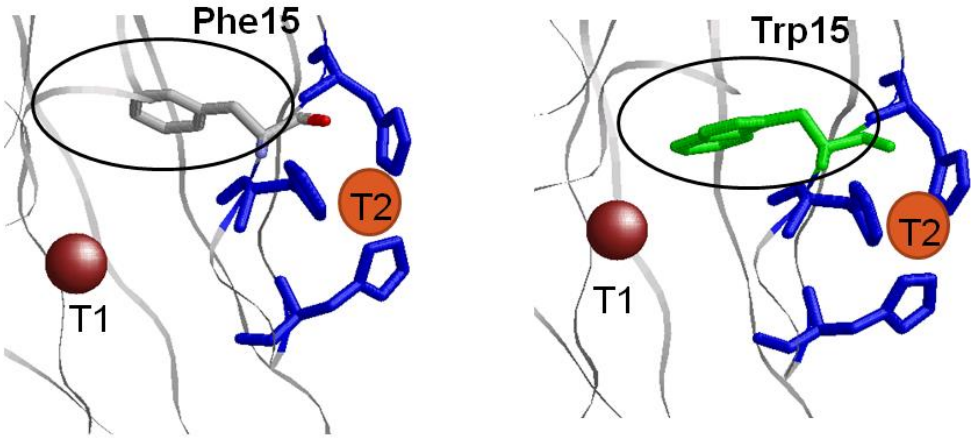

Figure 10 – The mutation of Phe15 into Trp15 for the NiR3His model.

After all three of these 2nd generation variants had been created individually, the mutations were doubled and tripled on top of each other creating variants such as NiR3His Phe15Trp; Phe114Pro and NiR3His Phe15Trp; Phe114Pro; Met121Gln. This

was done to see what effects doubling and tripling of these mutations on top of each other had on our models ability to mimic native nitrite reductase.

The characterization of these variants using EPR and UV-Vis spectroscopy will be covered in chapters 3 and 4. Chapter 5 will discuss the initial kinetic results for the activity of a select few of these variants in reducing nitrite. Chapter 2 will discuss the methods used for purifying and preparing samples as well as the experimental methods used for activity assays.

2.1 Creating New Variants: Mutagenesis:

New variants were created by adding second and third mutations to azurin variants that had been previously prepared, such as taking the NiR3His Phe15Trp variant and adding the Met121Gln mutation to it creating the NiR3His Phe15Trp Met121Gln double variant. This was performed using Stratagene QuikChange© site-directed mutagenesis. These variants were created for all four of the parents to create 16 new variants total.

After Stratagene QuikChange© site-directed mutagenesis reaction, plasmid copying by the DNA polymerase was confirmed by an agarose gel with the product against a 1 kb ladder as shown below in Figure 11.

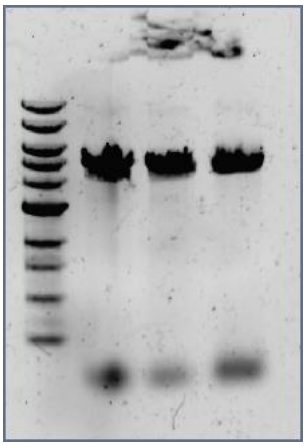

Figure 11- The product of the Stratagene QuikChange© site-directed mutagenesis for the variants NiR3His F15WF114P, NiR3His F15WM121Q and NiR3His F114PM121Q respectively. Shown is one large band at around 4.7 kb as well as a band below 0.5 kb which is due to digestion of the product by Dpn1 which cuts methylated DNA and is also due to excess primers in the reaction.

Restriction digest sites were also previously designed into the primers to either add or remove restriction enzyme cut sites. The two restriction enzymes utilized were SmaI and PstI. When the variants with multiple mutations were created, these

restriction digest sites were unaffected, allowing the use of previous restriction enzymes for the new variants. As an example, variants containing the Phe114Pro mutation used the enzyme SmaI. The enzyme SmaI could then be used for the variants containing Phe114Pro+Phe15W as well as the variant Phe114Pro+Met121Gln.

Variants supposed to contain the Phe114Pro mutation were digested using the SmaI restriction enzyme. The mutation of Phe114Pro removed a cut site for SmaI and changed the cut pattern from 2 bands located at 3.2 kb and 1.1 kb for the template plasmid without the mutation, to 1 band located at 4.7 kb for plasmids with the mutation. A positive result can be seen in figure 12 below, where lanes 2 and 3 are successful mutations and lane 4 is the un-mutated template.

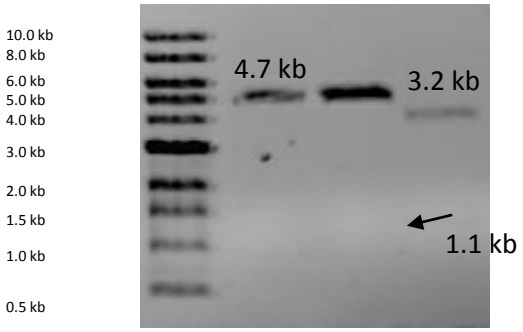

Figure 12- The creation of NiR F15WF114P DNA was initially confirmed in this miniprep digest. Lane 1 is the ladder, lane 2 and 3 are DNA miniprep samples digested with SmaI and lane 4 is the NiR3His F15W template DNA also digested with SmaI.

Variants supposed to contain the Met121Gln mutation were digested using the PstI restriction enzyme. This mutation added a cut site for PstI and changed the cut pattern from 1 band located at 4.7 kb for the template plasmid without the mutation to 2 bands located at 4.3 kb and 0.4 kb for plasmids with the mutation. A typical positive result can

be seen in figure 13 below with lanes 2-4 plasmids with the mutation and lanes 5 and 6 the template plasmid without the mutation.

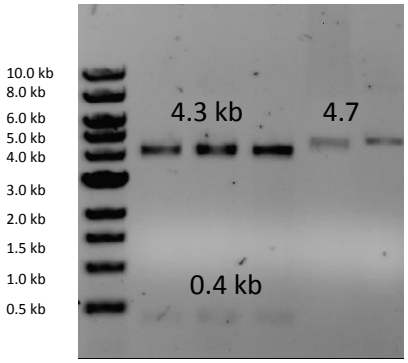

Figure 13 – Cut pattern of a PstI digest. Lanes 2,3 and 4 are variants that contain the M121Q mutation and were digested with PstI. Lanes 5 and 6 are the template DNA cut and then uncut respectively. In the lanes with the M121Q mutation, a 400bp band is clearly seen while there is no such band in the template DNA, confirming the presence of the M121Q mutation.

The pET9a plasmid that the azurin gene is located in contains a kanamycin resistance gene which allows for preferential growth and selection of successfully transformed cells in both the XL1-Blue *E. coli.*, as well as the BL21* (DE3) *E. coli*.. After DNA was produced with the QuickChange © mutagenesis process, it was then transformed into XL1-Blue *E. coli.*. Since XL1-Blue *E. coli.* do not contain a resistance to the antibiotic kanamycin and our plasmid does, transformation products were grown on LB plates containing the antibiotic kanamycin. This allowed for the selective culture of only cells that had taken in our plasmid DNA. XL1-Blue *E. coli.* were then utilized to produce large amounts of our plasmid DNA. This was accomplished with the IBI Midi Fast Ion Plasmid kit. Typical yields of 250 ng/uL of pure plasmid DNA was obtained. This DNA was then checked again using the same restriction enzymes as before to confirm that the correct plasmid was present.

Final confirmation that the DNA had the correct mutations was accomplished by Sanger sequencing performed by the University of Minnesota BioMedical Genomics center. This was performed for all variants and typical results translated from nucleotides into amino acids are shown below in Figure 14.

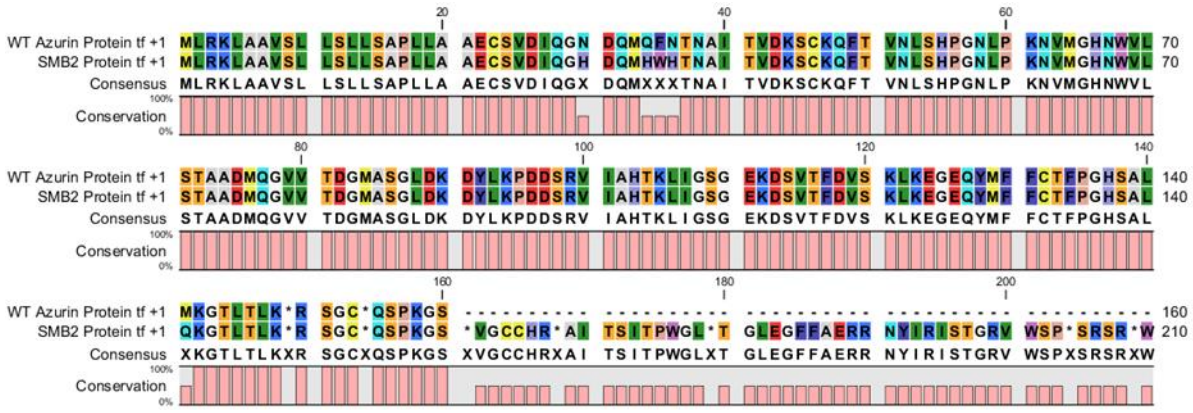

Figure 14 – The amino acid sequence alignment for the midiprep DNA of NiR3His F15WM121Q, performed by the software program CLC Viewer. WT sequence is the top row labeled WT Azurin Protein tf +1, NiR3His F15WM121Q is labeled SMB2 tf + 1. Bars below the sequence visualize where mutations have occurred.

Figure 14 above shows how the sequence results were interpreted. The top row of residues labeled "WT Azurin Protein tf + 1" corresponds to the amino acid sequence of wild type azurin. The second row is the experimental Sanger sequencing results for our NiR3His Phe15Trp Met121Gln model. Azurin starts at amino acid number 21 in the figure, with the first 20 amino acids being a leader sequence responsible for directing transport of the protein into the periplasmic space when the genes are expressed using *E. coli*..[20]

Once positive confirmation that the correct mutations are in place, the DNA was transformed into BL21* (DE3) *E. coli*., where again the kanamycin resistance imparted by the pET9a plasmid allows for selective growth on kanamycin LB –agar plates of cells that have taken in our plasmid DNA. The BL21* (DE3) *E. coli*. infected with our plasmid were then used to express the desired protein with the help of a T7 promoter induced by IPTG. The protein was then extracted from the cells via osmotic shock and purified using SP and Q sepharose ion exchange columns.

2.2 UV-Visible Absorption Spectroscopy Sample Preparation:

All proteins were expressed in BL21* *E. coli.* and purified as apo protein. In order to populate the azurin models with copper a titration was performed. To populate both copper centers in our models we used the following procedure. Apo protein had 5 equivalents of copper sulfate, added 1 equivalent at a time with stirring over ice. The sample was then left to sit for 20 minutes on ice to ensure complete binding of the copper to the protein. The now copper bound protein then had its buffer exchanged into 50 mM ammonium acetate at a pH of 5.1 buy running it through a PD-10 size exclusion column, packed with Sephadex G-25 M, 1 mL at a time and the blue fraction collected. The protein was then brought to a concentration of 200 µM and an absorbance spectrum was collected on a Shimadzu UV-2401 PC UV-Vis spectrophotometer. Since the Type 1 copper site has an absorptivity of 100 times that of the Type 2 copper site, only the Type 1 copper is observed for these samples. Spectra were measured of the Type 1 copper for all parent and second generation variants.

To create Type 2 copper only azurin samples, we first populated the Type 1 copper site with a Hg(II) ion. Samples were prepared by addition of 1.5 equivalents of $HgCl_2$ to a sample of greater than 500 µM apo protein and the $A_{280\ nm}$ was determined. The protein was then run through a PD-10 size exclusion column packed with Sephadex G-25 M and equilibrated with 50 mM ammonium acetate at a pH 5.1 and collected in three drop fractions. The fractions containing an $A_{280\ nm}$ peak were then collected and the concentration of the protein was estimated based on the amount of dilution of the $A_{280\ nm}$ peak. If the protein was less than 500 µM it was concentrated using a 3000 NMWL Ultracell® YM membrane Centricon centrifugal filter device until it was greater than 500 µM. Less than one equivalent of copper was then added to the protein and the absorbance spectrum was measured. Spectra have only been measured of the Type 2 copper centers the parent variants so far. It should be noted that the absorptivity for Type 2 copper centers is typically less than 100 $M^{-1}cm^{-1}$ for each of the parents, so a 250 µM sample has an absorbance of less than 0.05. Also that the apo protein has a slight baseline absorption so a spectra of the apo protein needs to be subtracted.

2.3 EPR Spectroscopy Sample Preparation and Parameters:

EPR samples were all prepared to incorporate only a Type 1 copper, a Type 2 copper or both a Type 1 and Type 2 copper. To get a spectrum for both the Type 1 and the Type 2 copper, 5 equivalents of $CuSO_4$ was added slowly over ice with gentle stirring. This consisted of adding 1 equivalent over a period of 1 minute, 5 times. The sample was then let to sit for 20 minutes to ensure complete copper binding. The copper bound sample

was then run down a PD-10 size exclusion column packed with Sephadex G-25 M 1mL at a time and the blue fraction was collected. The collected fraction was then concentrated to 2 mM and in a volume of 150 µL using a Millipore 3000 NMWL Ultracell® YM Centricon centrifugal filter device. This 150 µL was then mixed into 150 µL of glycerol and vortexed quickly before being tranferred into EPR tubes with a syringe and nylon needle, and flash frozen in liquid N_2. To get a signal from only the Type 1 copper site, 0.75 equivalents of copper sulfate was added instead of the 5 equivalents used for the Type 1 and Type 2 copper sample. The rest of the procedure was the same.

To make samples with only the Type 2 copper center populated, 1.5 equivalents of $HgCl_2$ was added to occupy the Type 1 copper site and prevent copper from binding. After adding mercury, the sample was let sit for 20 min on ice to ensure complete binding. After 20 minutes the sample $A_{280\ nm}$ was recorded before passing through a PD-10 size exclusion column similar to the copper bound samples. With mercury bound in the Type 1 site no blue color is observed. Because of this 3 drop (approximately 150 µL) fractions were collected in 25 vials and each checked for $A_{280\ nm}$. Only samples with an $A_{280\ nm}$ of more than 0.25 A.U. were kept. These fractions were then combined and the total concentration was based on the total $A_{280\ nm}$, comparing the final $A_{280\ nm}$ to the initial $A_{280\ nm}$ and using this ratio to calculate the new concentration. This sample was then concentrated using a Millipore Centricon to a final volume of 150 µL and a final concentration of 2 mM. This 150 µL was then mixed with 150 µL of glycerol and 0.5 equivalents of $CuSO_4$ was added so that copper could then bind to the unoccupied Type 2

copper site. Finally the solution was syringed into an EPR tube and flash frozen into liquid N_2.

EPR spectra were measured for all of the parent and second generation variants. Samples were run at 77 K on a Varian E-Line Century Series X-band EPR spectrometer. The frequency was set to 9.27 GHz with a center field of 3000 gauss. A field sweep of 1600 gauss was taken over 60 seconds with 2 scans averaged per spectra. A wait time of 10 seconds was set between scans with the modulation amplitude set to 5 and a time constant of 0.032. Fifteen spectra were taken for each variant and averaged for simulation using Simpow 6.

2.4 Griess and Reoxidation Assay Sample Preparation:

Apo protein was titrated with copper by slow addition of 5 equivalents of $CuSO_4$ while mixing with a stir bar on ice. Initially, one equivalent was estimated via the protein's absorbance at 280 nm with an absorptivity of 8440 $M^{-1}cm^{-1}$. A small aliquot of apo protein is removed, usually around 100 µL, and $^1/_{10}$ to $^1/_4$ equivalent (based on the A_{280nm} and ε = 8440 $M^{-1}cm^{-1}$) of $CuSO_4$ is added stepwise and the absorbance max located at around 625 nm (variant dependent) is monitored. When addition of $CuSO_4$ yields no further increase in the ~625 nm maximum, the exact concentration of protein is determined based on the ~625 nm peak and an absorptivity of 5000 $M^{-1}cm^{-1}$. From this concentration, 5 equivalents of copper sulfate is determined. It should be noted that 2 equivalents of the 5 equivalents of Cu(II) are required to fully bind Cu(II) to the protein, since a single Cu(II) is required for each of the type one and type two sites. The excess of Cu(II) is used to ensure full saturation (3 equivalents beyond the 2 equivalents needed).

After the addition of copper sulfate, the protein is run through a PD-10 column, in a volume of no more than 1 mL at a time, to exchange the buffer into 20 mM phosphate at a pH of 6.35 as well as to remove any excess copper that is unbound to protein. The concentration of this holo protein is determined again using the absorbance maximum at ~625 nm. Finally the protein is diluted to a concentration of

100 µM in 260 µL and is aliquoted out into screw cap vials and flash frozen in liquid N_2. These samples give a final protein concentration of 86 µM after addition of 30 µL of nitrite and 10 µL of ascorbate to begin the assay.

2.5 Griess Assay Methods:

For Griess assays, previously prepared protein samples were brought into the glove box approximately 20 min before the assay began and left to sit and stir with the lid open to thaw and achieve anaerobic conditions and to also let the temperature equilibrate up to room temperature. After this time, 30 µL of varying nitrite concentrations were added (see Table 1 for exact amounts and concentrations). The sample was mixed for 5 minutes by stir bar to ensure complete mixing of nitrite in the sample. Initial data points were removed and reacted with Griess reagents before the addition of ascorbic acid to confirm that the right amount of nitrite was added and that the right concentration of nitrite was present. Then 10 µL of 1 M ascorbic acid was added (final concentration of 33 mM) to reduce the protein and initiate the reaction and data points were collected every 10 – 15 min (see Table 1) until a ~5% decrease in nitrite was observed (which is the same as a 5% decrease in the A_{540} of the Griess reaction). Data points were obtained by removing

20 µL from the reaction vessel and diluting them into buffer, various dilutions were used based on the concentration of nitrite present in the sample (see Table 1 below). For all assays except the 2, 5 and 10 mM NO_2^-, the final nitrite concentration before Griess reaction was no more than 40 µM, which gives a final absorbance of at most 0.7 A.U.. However, for the 2, 5 and 10 mM NO_2^- samples it was too complicated to dilute to the same reacted concentration of nitrite, so 20 µL of the reaction mixture was only diluted into 480 µL of buffer and then reacted with Griess reagents. This yields nitrite concentrations before the Griess reaction of 80, 200 and 400 µM nitrite. These must then be diluted down after the reaction to get into a reasonable absorbance for measurement (see Table 1). This is possible because even at the highest concentration, the 10 mM nitrite with a reacted concentration of 400 µM nitrite, the NED is still in ~10 times excess and the SAN is in ~145 times excess (2.88E-5 moles SAN, 1.93E-6 moles NED and 2E-7 moles NO_2^-). There also remains a linear trend in the absorbance observed up to the 10 mM nitrite starting concentration which has a reacted nitrite concentration of 400 µM as shown in Figure 15.

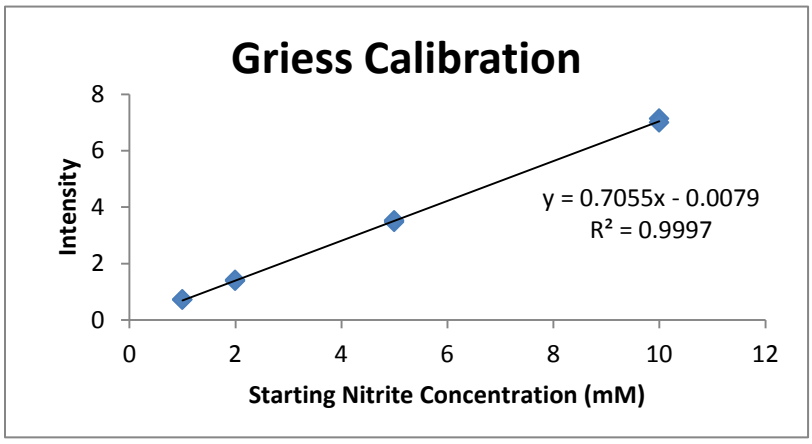

Figure 15 – The calibration plot for Griess assay absorbance vs. nitrite concentration for [NO_2^-] of 1-10 mM.

After the nitrite was diluted to a concentration that would yield an appropriate absorbance, a volume of 500 µL of the diluted sample was reacted with 500 µL of sulfanilic acid (SAN). This was vortexed briefly (about 3-4 seconds) and then 500 µL of N-(1-naphthyl)ethylenediamine (NED) was added and the mixture was vortexed again for 5 seconds.

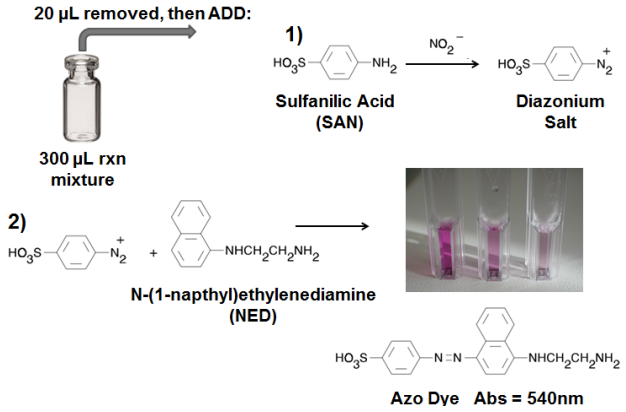

Figure 16- Griess reaction scheme.

Care must be taken to add the NED as quickly as possible after adding SAN since the presence of ascorbate can inhibit color formation after SAN is added through the reaction of ascorbate with the diazonium salt (see Figure 17). This was shown by Moody with their graph demonstrating $A_{540\ nm}$ and the delay between SAN and NED additions in the presence of ascorbate, which resulted in a loss of over 75% of possible color formation after 20 minutes.[33]

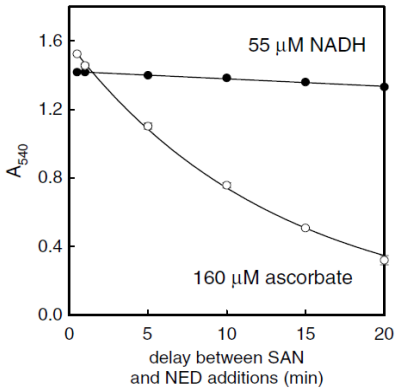

Figure 17 – The effect of time delay between the addition of SAN and NED to nitrite samples containing ascorbate. The white circles correspond to a sample that contained a 160 μM concentration of ascorbate, which is ~ 200 times lower concentration then is present in our assays.[33]

This mixture of the assay solution with Griess reagents was then left to sit for 10 minutes to ensure complete color formation was attained before the absorbance was taken. Samples have been shown to achieve full color formation in as little as 6-7 minutes and the color stays for up to 30 minutes for all samples except the methods used in the 5 mM and 10 mM nitrite assays. For the 5 mM and 10 mM nitrite samples, precipitants are formed if the undiluted reacted Griess sample is left to sit for longer than ~20 minutes. A wait of 10 minutes was used between the reaction and absorbance measurements to ensure that each trial was consistent. The azo dye formed has a maximum absorption at 540 nm and no absorption at 700 nm, so data points were taken as the difference between the peak at 540 nm and the absorbance at 700 nm.

Table 1 – dilutions and NO_2^- additions

Nitrite Concentration	Dilutions	Nitrite addition and time between data points
1 mM	20 µL of rxn assay was diluted into 480 µL of buffer and then reacted with Griess reagents and the absorbance taken after 10 min.	30 µL of 10 mM NO_2^- First point removed at 2 min, then every 10 min starting at 10 min
2 mM	20 µL of rxn assay was diluted into 480 µL of buffer and then reacted with Griess reagents. After 10 min for color evolution, 500 µL of this was then diluted into 500 µL of buffer and the absorbance taken.	30 µL of 20 mM NO_2^- First point removed at 2 min, then every 10 min starting at 10 min
5 mM	20 µL of rxn assay was diluted into 480 µL of buffer and then reacted with Griess reagents. After 10 min for color evolution, 200 µL of this was then diluted into 800 µL of buffer and the absorbance taken.	30 µL of 50 mM NO_2^- First point removed at 2 min, then every 10 min starting at 10 min
10 mM	20 µL of rxn assay was diluted into 480 µL of buffer and then reacted with Griess reagents. After 10 min for color evolution, 100 µL of this was then diluted into 900 µL of buffer and the absorbance taken.	30 µL of 100 mM NO_2^- First point removed at 2 min, then every 10 min starting at 10 min
25 mM	20 µL of rxn assay was diluted into 480 µL of buffer and then vortexed for 10 s. 20 µL of this was then taken and diluted into another 480 µL of buffer and reacted with the Griess reagents. After 10 min for color evolution the absorbance was taken.	30 µL of 250 mM NO_2^- First point removed at 2 min, then every 15 min starting at 15 min
50 mM	20 µL of rxn assay was diluted into 980 µL of buffer and then vortexed for 10 s. 20 µL of this was then taken and diluted into another 480 µL of buffer and reacted with the Griess reagents. After 10 min for color evolution the absorbance was taken.	30 µL of 500 mM NO_2^- First point removed at 2 min, then every 15 min starting at 15 min

100 mM	20 µL of rxn assay was diluted into 980 µL of buffer and then vortexed for 10 s. 20µL of this was then taken and diluted into another 980 µL of buffer and vortexed for 10 s. From this, 500 µL of sample was removed and pippeted into the waste and the remaining solution was reacted with the Griess reagents. After 10 min for color evolution the absorbance was taken.	30 µL of 1 M NO_2^- First point removed at 2 min, then every 15 min starting at 15 min
150 mM	20 µL of rxn assay was diluted into 980 µL of buffer and then vortexed for 10 s. 20 µL of this was then taken and diluted into another 980 µL of buffer and vortexed for 10 s. From this, 500 µL of sample was removed and pipeted into the waste and the remaining solution was reacted with the Griess reagents. After 10 min for color evolution the absorbance was taken.	30 µL of 1.5 M NO_2^- First point removed at 2 min, then every 15 min starting at 15 min

The Griess assay was performed for all four of the parent variants. It was determined that NiR3His had the highest activity for nitrite reduction, so the second generation NiR3His variants of NiR3His Phe15Trp, NiR3His Phe114Pro and NiR3His Met121Gln were the next three targeted for assays. The other variants will be assayed at a later time. After determining the rate of nitrite reduction for each variant and concentration of nitrite, the SigmaPlot 12.5 enzyme kinetics function was used to determine K_m and V_{max} values.

2.6 Reduction and Reoxidation Assay Methods:

Samples were prepared using the same method described above for the Griess assay and with the same concentration, however, samples were aliquoted into 2 mL volumes or greater because a larger cuvette was necessary to properly stir the sample. Before bringing the sample into the glove box, samples were degassed with argon for more than 5 minutes by bubbling in a 15 or 50 mL falcon tube. Samples were monitored at 625 nm every 2 seconds over approximately 90 minutes. The first step was to reduce the protein using ascorbate. This usually required around 2 equivalents of ascorbate

based on the concentration of the protein. After the protein was fully reduced, nitrite was added to final concentrations that ranged from 1 mM to 150 mM. The rate of reoxidation was determined by finding the linear region of reoxidation with the largest slope and an R^2 value as close to 1.00 as possible. This was usually around 4 or 5 minutes after reoxidation began and was linear for about 2 minutes total. The fits of a reoxidation assay are shown in Figure 18. To date, reoxidation assays have only been completed for the parent variant NiR3His.

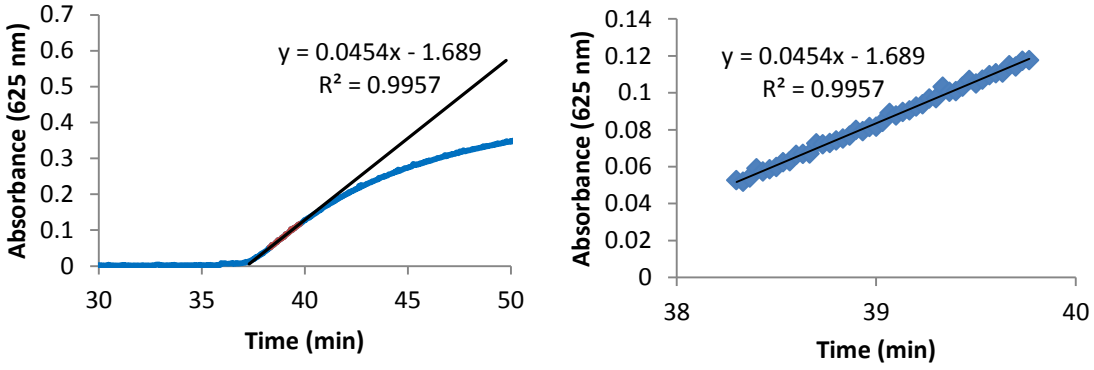

Figure 18 – Using a linear regression line to find the initial rate of reoxidation for a 100 µM NiR3His sample containing 50 mM nitrite after reduction with 2 equivalents of ascorbate. Left is the overall reoxidation and right is only the linear portion fit with a regression line.

2.7 Proof of Nitric Oxide production:

In two separate containers, a 5 mL solution of 0.1 M H_2SO_4 with 0.3 M $FeSO_4$ and a 0.5 M NaOH with 0.2 M EDTA were prepared. Each was degassed with argon before transfer to the glove box. This method was based on the paper *recipe for ferric salts of Ethylenediaminetetraacetic Acid* by Steiner, except all samples were prepared

anaerobically to prevent oxidation, which results in a yellow color and a complex that will not react with NO.[34] After being brought into the glove box, 600 µL of the EDTA solution was mixed with 400 µL of the $FeSO_4$ solution and put into a cuvette to form $[Fe(EDTA)]^{2-}$. This solution was used to blank the spectrometer. Next, 1 cc of gas from inside the glove box was then injected into the cuvette via syringe with a hypodermic needle 5 times. The spectra were recorded to check if any gas from the glove box resulted in a spectral change. This resulted in the pink spectra shown in Figure 19. Then, a 1 mL solution of 260 µM NiR3His with 100 mM NO_2^- was put into a sealed anaerobic vial with a septa and the reaction was initiated by injection of ascorbic acid to a final concentration of 30 mM via syringe. The reaction was let sit for 2 hours before 1cc of the headspace was removed by syringe and bubbled through the $[Fe(EDTA)]^{2-}$ solution, the resulting spectra is shown in blue below.

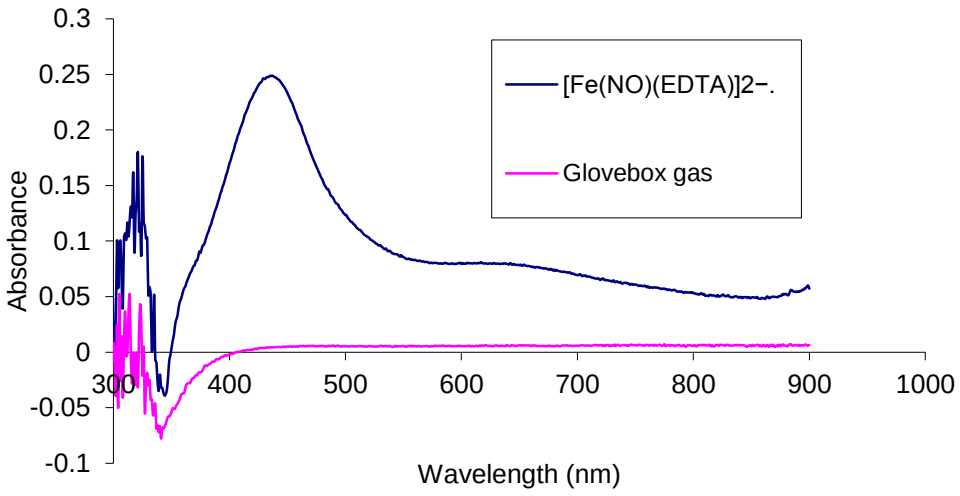

Figure 19 – Pink line is the gas from the glovebox bubbled through the $[Fe(EDTA)]^{2-}$ solution as a control. Blue line is the headspace gas from the sealed assay with NiR3His which when compared to the spectra given by Tegoni confirms that NO is a product.[35]

The results are comparable to what was seen by Tegoni in their detection of NO as a product of their protein mimic of a Type 2 copper site as seen in Figure 20.[35]

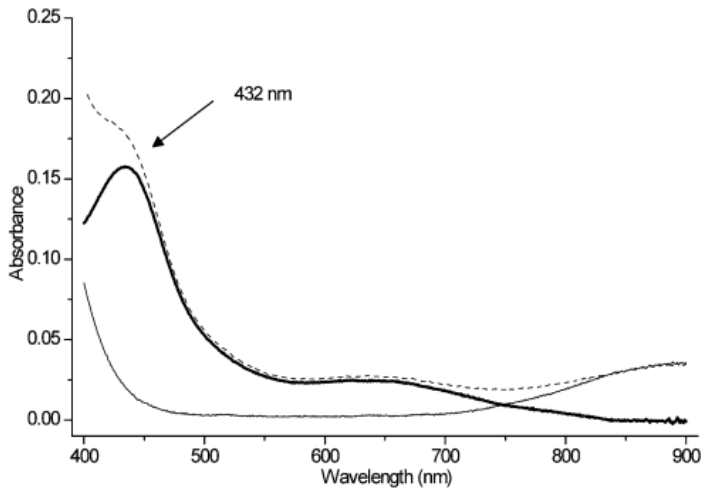

Figure 20 -The above spectra is taken from the Tegoni paper and was used to confirm that $[Fe(NO)(EDTA)]^{2-}$ was produced.[35] The thin line is the spectra of $[Fe(EDTA)]^{2-}$ in 1M citrate buffer, the dashed is the spectra after flushing with gas evolved from the reaction and the dark line is the difference.

Chapter 3: Enzyme Kinetics

3.1 Assay Calibrations and Controls:

The first method used to determine the kinetic activity of our models was the Griess assay. This technique reacts nitrite with sulfanilic acid (SAN) to form a diazonium salt. This salt is then reacted with N-(1-naphthyl)-ethylenediamine (NED) to form an azo dye that has an absorbance maximum at 540 nm.[36,37] As our reaction proceeded, aliquots of the sample were removed and reacted with SAN and NED to determine the nitrite concentration present. The nitrite concentration plotted versus times gives the initial rate for the loss of nitrite. When these rates are plotted versus their respective nitrite concentrations, the data can be fit with the Michaelis-Menten model described by Equation 3, which is derived from Equation 2.

$$E + S \underset{k_r}{\overset{k_f}{\rightleftarrows}} ES \xrightarrow{k_{cat}} E + P \tag{2}$$

$$V = \frac{V_{max}[S]}{K_m + [S]} \tag{3}$$

To start out, we needed to determine the relationship between the absorbance of the Griess assay and the concentration of nitrite present in our samples. Shown in Figure 21 is the absorbance of the Griess assay at four different concentration of nitrite, 1, 2, 5 and 10 mM. At concentrations above 10 mM nitrite, the azo dye product that formed from the Griess reactions precipitated, which led to non linear absorbance results. We therefore developed a procedure of diluting our high nitrite concentration reaction

aliquots in buffer to a concentration below 10 mM nitrite before reacting them with the Griess reactants. The slope of the calibration plot (Figure 21) was used to determine the concentration of nitrite present in our samples and demonstrates the linear correlation between the absorbance at 540 nm and the concentration of nitrite present for samples between 1 and 10 mM nitrite.

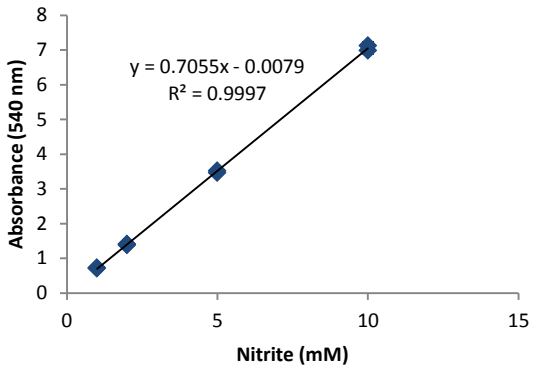

Figure 21 – Calibration plot for the absorbance of the Griess reagents over a range of nitrite concentrations

It was also necessary to confirm that any decompositions of nitrite observed was due to only our enzyme and not any background rate where nitrite is reduced directly by ascorbic acid. To do this, an assay was conducted in a sample containing 20 mM phosphate buffer at a pH of 6.35, 100 mM nitrite and 33 mM ascorbic acid. The results are shown in Figure 22 and indicate that the background rate at the very high concentration of 100 mM nitrite gives a rate of 0.0002 ± .00011.5 mM A.U./min. This rate is approximately 100 times slower than the rate observed at the same nitrite concentration and pH as our NiR3His variant, which led to the conclusion that the background reaction is insignificant relative to the protein catalyzed reaction.

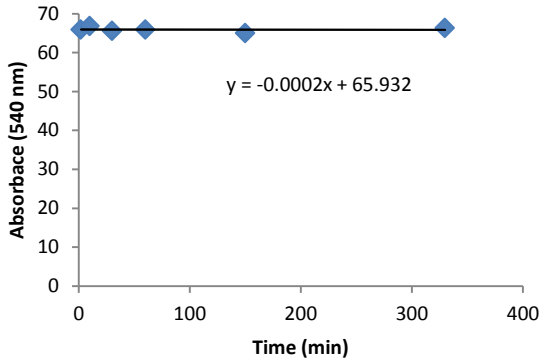

Figure 22 – Background reaction rate of 100 mM nitrite with 33 mM ascorbic acid in 20 mM phosphate buffer at pH 6.35. The slope of the trendline is in A.U./min

A second control conducted tested our template protein azurin. For this control a sample of wild type azurin was prepared and the activity tested using the Griess assay. The results shown below in Figure 23 are reduction rates for wild type azurin at four nitrite concentrations. The lack of activity confirms that the Type 1 copper site in azurin has negligible contribution to the reduction of nitrite by itself.

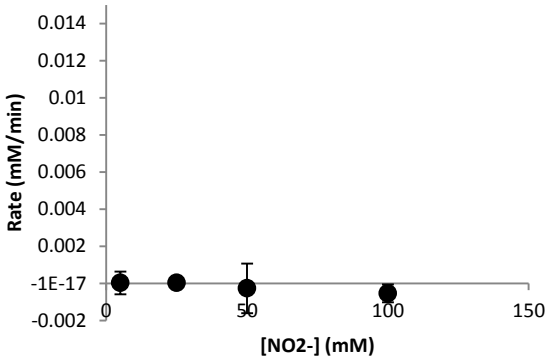

Figure 23 – Wild Type type 1 azurin nitrite reductase activity rates. Sample contained 86 µM azurin, 5-100 mM nitrite and 33 mM ascorbate in 20 mM phosphate buffer at pH 6.35.

Next we needed to determine if the ionic strength of the reaction solution affected the rate of nitrite reduction. This was determined by varying the nitrite concentration and adding NaCl to keep the total ionic strength of NaCl in combination with $NaNO_2$ at a constant value, and comparing these rates to the rates when no NaCl is present. As can be seen in Figure 24, where the blue line is the Michaels-Menten fit for NiR3His that will be described later, and the black dots are assay rates for samples with a 100 mM total ionic strength, there appeared to be no loss of activity between samples with and without NaCl in the reaction mixture.

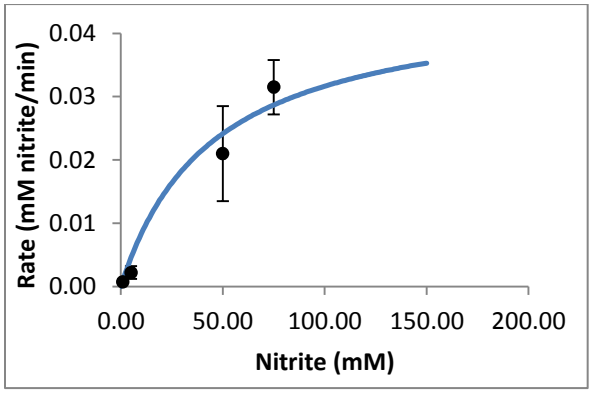

Figure 24 – 86 µM NiR3His assayed using the Griess reaction at various nitrite concentrations. Samples were in 20 mM phosphate buffer at pH 6.35 with NaCl added for a total ioninc strength of NaCl + $NaNO_2$ of 100 mM. Blue line is Michaelis-Menten fit for assay samples and black dots are samples with NaCl to increase the ionic strength.

Since the goal of the Griess assay is to apply Michaelis-Menten kinetic to these models, it is also required that the reducing agent be in excess. This is necessary as it is an assumption under the Michaelis-Menten model that the concentration of active, reduced enzyme,[E] in Equation 2, remains constant over the entirety of the reaction.[38]

The only loss of enzyme should be due to the formation of an enzyme-substrate complex, [ES], which after either substrate dissociation or product formation and dissociation, returns to the reduced active form. To determine what constituted an excess of reductant, a range of ascorbate concentrations, from approximately 16 mM to 60 mM was tested in a Griess assay of the NiR3His variant over 1300 minutes. As can be seen in Figure 25, there was no distinguishable difference between any of the concentrations used over that time period. Since our assay procedure calls for an initial concentration of 33 mM ascorbate, it can be concluded that we have ascorbate in excess for our reactions. Had ascorbate not been in excess, a faster rate of the nitrite concentration loss would have been observed as the concentrations of ascorbate increased.

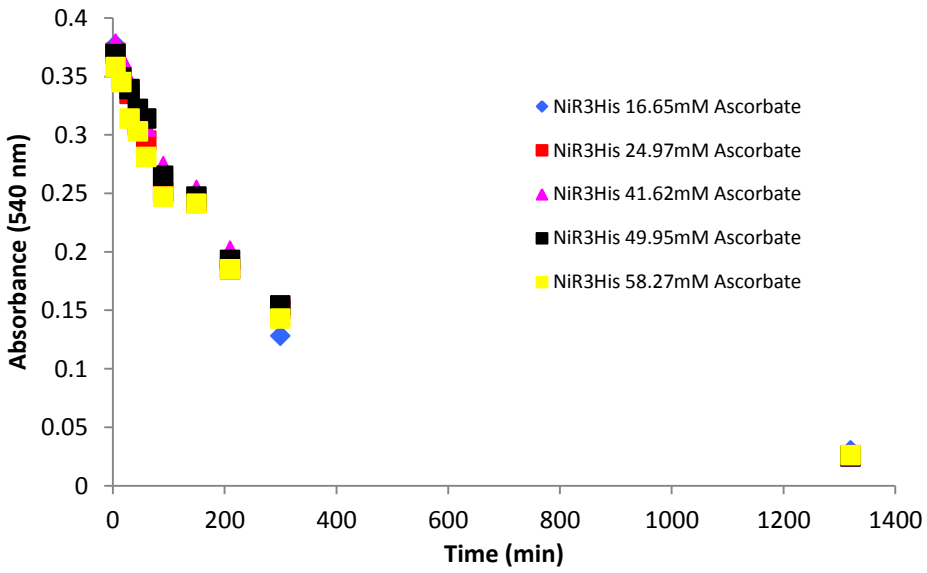

Figure 25 – Varied ascorbate concentrations in an assay with NiR3His. Enzyme concentration was 86 µM with 1 mM nitrite in 20 mM phosphate buffer at pH 6.35.

3.2 Griess Assay Michaelis-Menten Results:

The Michaelis-Menten kinetics for each of the variants was determined by using the initial slope of the first 5% loss of nitrite in the reaction mixtures. An example of one assay is

shown in Figure 26, with each data point being an individual aliquot of the reaction mixture removed at a given time.

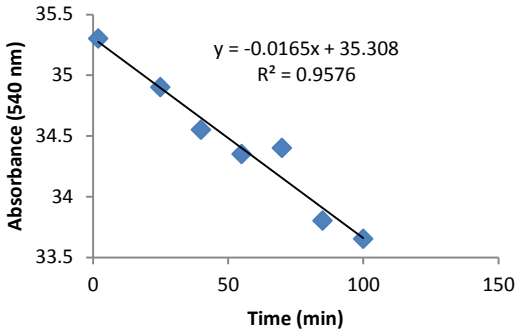

Figure 26 – The initial rate of the loss of nitrite in 86 µM NiR3His sample with 50 mM nitrite as monitored by the Griess assay. The sample was reduced with 33 mM ascorbate and in a 20 mM phosphate buffer at pH 6.35.

Each of these individual assays was repeated in triplicate for the parent variants at a range of nitrite concentrations from 1 mM up to 150 mM. These rates were then plotted versus their nitrite concentrations as shown in Figures 27 and 28, and Michaelis-Menten

values of K_m and V_{max} were determined using the Sigma Plots 12.5 enzyme kinetics tool. The K_m and V_{max} values for each parent are shown in Table 2 below.

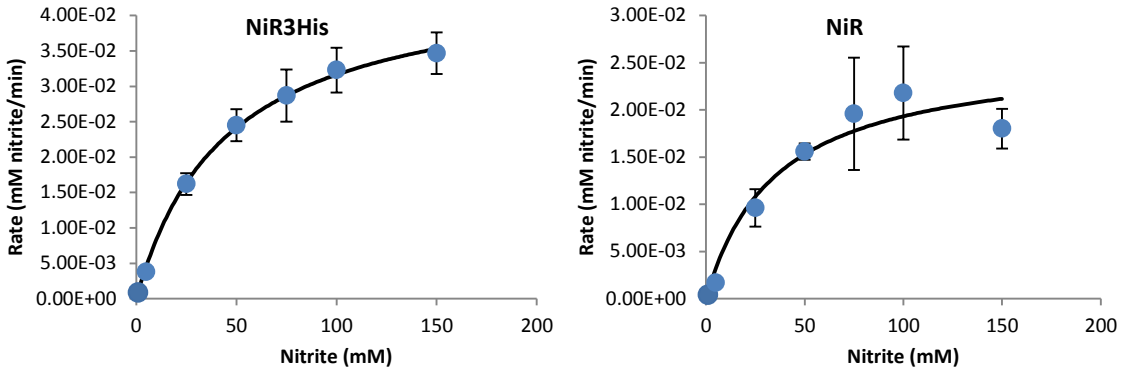

Figure 27 – Michaelis-Menten plots for the NiR and NiR3His parent variants.

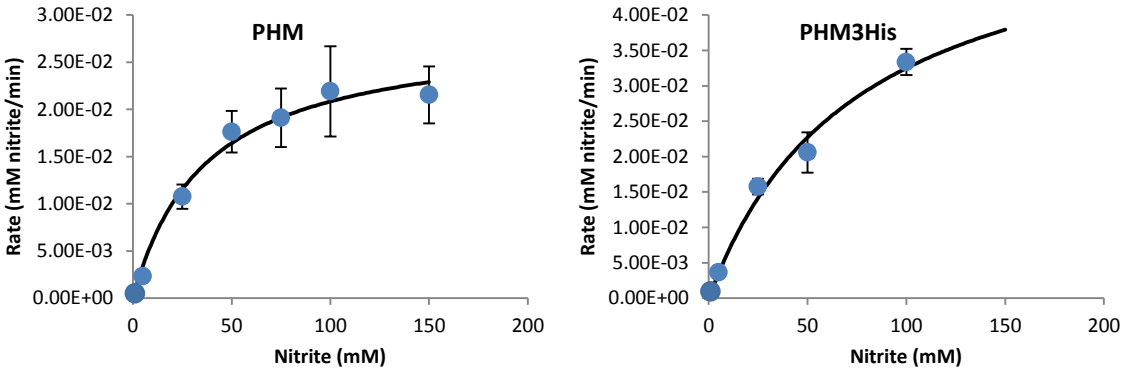

Figure 28 – Michaelis-Menten plots for the PHM and PHM3His parent variants.

Table 2 – K_m and V_{max} values for our four parent variants as well as the values for the native NiR from *Alcaligenes faecalis* at a comparable pH of 6.5.[3]

Variant	K_M (mM Nitrite)	V_{max} (mM nitrite / min)	Turnover Number (s^{-1})
NiR3His	45 ± 12	$4.59*10^{-2}$ ± 0.0046	$8.90*10^{-3}$
NiR	35 ± 22	$2.62*10^{-2}$ ± 0.0054	$4.37*10^{-3}$
PHM3His	75 ± 22	$5.70*10^{-2}$ ± 0.019	$1.10*10^{-2}$
PHM	36 ± 16	$2.85*10^{-2}$ ± 0.0044	$5.52*10^{-3}$
Native NiR From *A. f.*[3]	0.053 ± 5	Not Listed	1046 ± 33

Our four parent variants all produced comparable K_m values on the order of 1000 times greater than that of *Alcaligenes faecalis*, a native NiR assayed at a comparable pH comparable to our system.[3] This indicates that our parent variant models have a much weaker binding affinity for nitrite than that of native NiR's. The turnover numbers for each parent were also 10^6 times slower that of the native NiR from *Alcaligenes faecalis*. To improve on our models K_m and turnover numbers, three additional mutations were made to produce the "second generation" variants.

3.3 Second Generation Variants Kinetics:

To improve on K_m and V_{max} for the four parent variants, the three "second generation" mutation sites were designed. These variants were designed to either lower the reduction potential of the Type 1 copper to better match that of native nitrite reductase as in the Phe114Pro and Met121Gln variants, or to aid in the transfer of an electron from the Type 1 copper to the Type 2 copper as in the Phe15Trp variant as mentioned in chapter 1 section 4. Figure 29 shows the Michaelis-Menten plots for the second generation variants of NiR3His with K_m and V_{max} for each listed in Table 3. The kinetics of second generation variants for the remaining parents are still being determined.

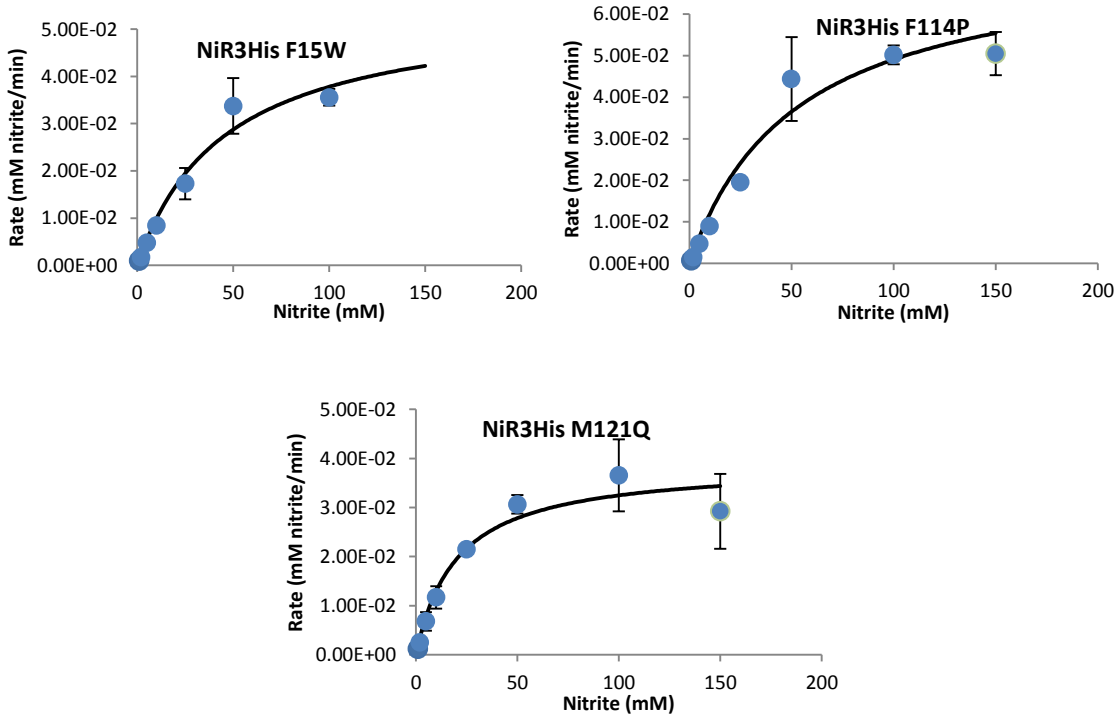

Figure 29 – MM plots for the three NiR3His second generation variants.

Table 3 – K_m and V_{max} values for the second generation variants.

Variant	K_M (mM Nitrite)	V_{max} (mM nitrite / min)	Turnover Number (s^{-1})
NiR3His F15W	46.05 ± 15.66	$5.52*10^{-2}$ ± 0.0087	$1.07*10^{-2}$
NiR3His F114P	52.55 ± 17.40	$7.49*10^{-2}$ ± 0.0105	$1.45*10^{-2}$
NiR3His M121Q	20.00 ± 7.38	$3.90*10^{-2}$ ± 0.0043	$7.66*10^{-3}$

It appears that there was a slight improvement in the K_m for the NiR3His M121Q variant, decreasing from 45 mM for NiR3His down to 20 mM for NiR3His M121Q, indicating twice the affinity for binding substrate. There was also a 1.5 fold increase in the turnover number for the F114P variant of NiR3His compared to the parent NiR3His.

While it does appear that these mutations did have a slight effect on the activity of our model, they were unable to generate any significant increase in the activity when compared to native nitrite reductases. However, our ability to rationally design a Type 2 copper center in azurin that yields nitrite reductase activity, albeit much less than the native system, gives promising hope that future designs will further improve on our models.

3.4 Catalysis and Pseudo-First Order Reoxidation Assays:

Since the Griess assays followed only the nitrite concentration, it was important to know what was happening to our enzymes during the reaction. In order to get an insight into what our enzyme was doing over the course of nitrite reduction, we needed to use as

assay which directly monitored the concentration of the oxidized form of our enzyme, termed a reoxidation assay. This assay follows the oxidized form of our Type 1 copper sites which has an absorbance maximum at 625 nm. This absorbance is lost upon reduction of the Type 1 copper site into the reduced, Cu(I), form. The figure below shows the absorption at 625 nm of the NiR3His variant as it is repeatedly reduced with ascorbate and then allowed to reoxidize in the presence of excess nitrite. A similar procedure was demonstrated by Tegoni for their model of a Type 2 copper center designed into a *de novo* peptide.[35] Our NiR3His sample was reduced by ascorbate and then reoxidized by nitrite 6 times in 500 minutes and regained 100% of its initial absorbance after 24 hours (shown as the red square in Figure 30) indicating our model can effectively act as a regenerable catalyst.

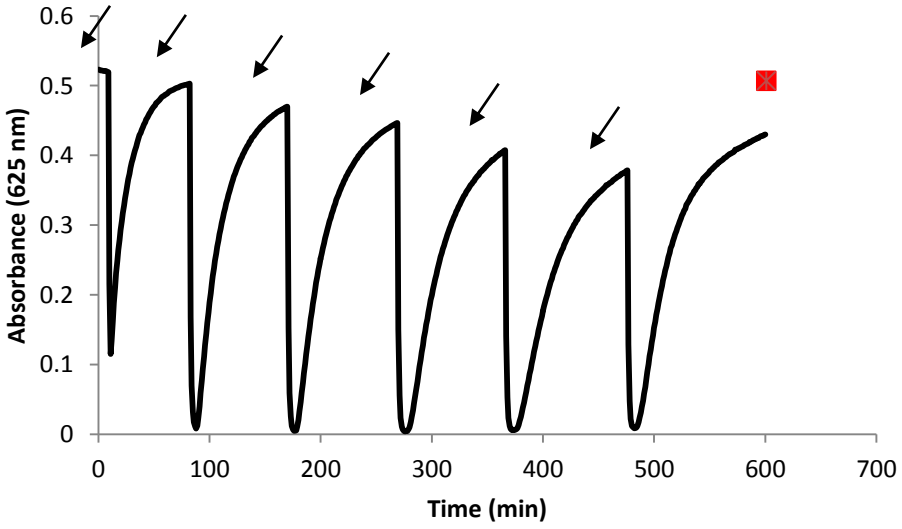

Figure 30 – A 100 µM sample of NiR3His was reduced with 2 equivalents of ascorbate, as indicated by the arrows, in the presence of 10 mM nitrite. After 30-100 min the sample was then reduced again with an additional two equivalents of ascorbate. The red square is the absorbance after letting the sample sit for an additional 24 hours. Samples were under anaerobic conditions in 20 mM phosphate buffer at pH 6.35.

To determine if the reoxidation of the protein is due to nitrite, and not another reaction, a reoxidation experiment similar to the one in Figure 30 was performed with nitrite added after the sample had been reduced for a period of time as shown in Figure 31.

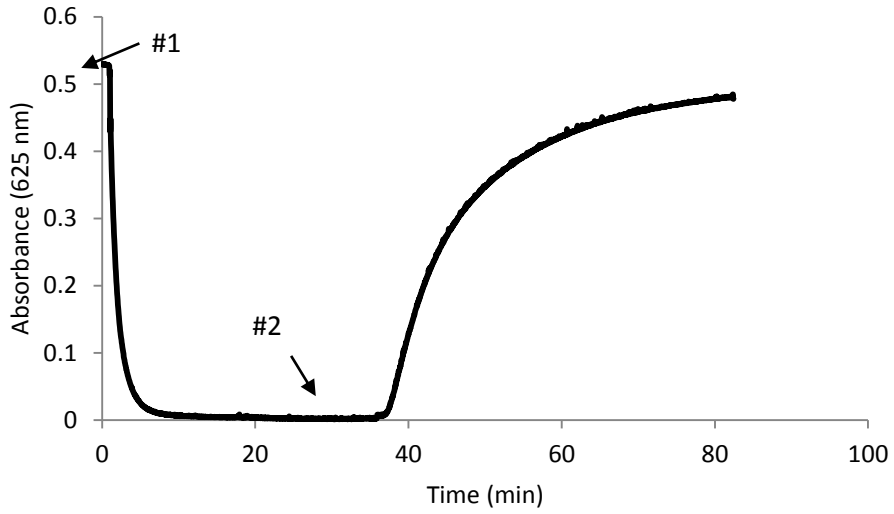

Figure 31 – 100 µM NiR3His reduced with 2 equivalents of ascorbate indicated at arrow #1 and then reoxidized using 500 equivalents (50 mM) of nitrite indicated at arrow #2. Sample was under anaerobic conditions in 20 mM phosphate 6H 6.35.

Above, the sample was reacted with 2 equivalents of ascorbate and allowed to fully reduce. The sample then sat for 30 minutes before nitrite was added. Had our enzyme reoxidized before the addition of nitrite, we would have concluded that our protein was being reoxidized by some other means than from nitrite. An example of this is when the reaction mixture is not fully deoxygenated, and then O_2 reacts with our Type

1 copper center, reoxidizing it without the presence of nitrite. Additionally, in doing this experiment it was noted that the rate at which the protein reoxidizes after the addition of nitrite is initially linearly dependent on the concentration of nitrite in the reaction. This means that the reoxidation rates are pseudo-first order, with the reaction being overall first order with respect to nitrite. Shown below is an example of how the rate of reoxidation was determined.

As a control, a reoxidation assay was performed on wild type azurin. In this assay, wild type azurin was reduced with 2 equivalents of ascorbate. Nitrite was then added (arrow #1 in Figure 32) to a final concentration of 10 mM to see if this would induce reoxidation. When no reoxidation occurred after 100 minutes, one extra equivalent of copper was added (arrow #2 in Figure 32) to determine if unbound copper in the presence of our reduced protein could also induce reoxidation of our protein by nitrite. Again, no reoxidation occurred for 100 minutes indicating nitrite does not oxidize the Type 1 copper site in azurin even in the presence of unbound copper. This indicates that copper bound to the Type 2 copper site is essential for the reoxidation of the Type 1 copper sites in our models.

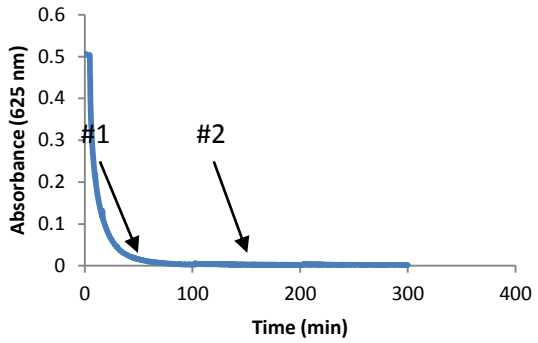

Figure 32 – Reoxidation assay with 100 µM wild type azurin reduced by 2 equivalents of ascorbate. Arrow 1 indicates the addition of 10 mM nitrite. Arrow 2 indicates the addition of 1 equivalent of excess $CuSO_4$. Sample was under anaerobic conditions and in 20 mM phosphate buffer at pH 6.35.

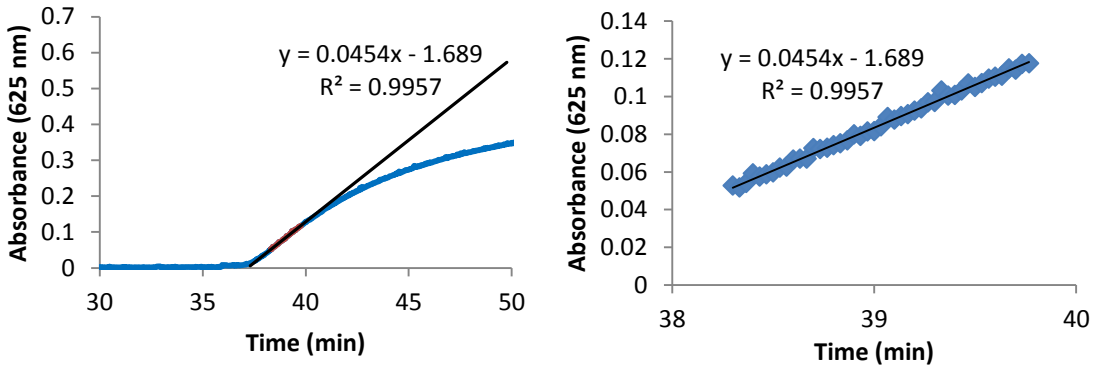

Figure 33 – The initial rate of reoxidation of 100 µM NiR3His in the presence of 50mM nitrite. Left shows the overall reoxidation and right shows Sample was under anaerobic conditions in 20 mM phosphate buffer at pH 6.35.

After samples began to reoxidize, the rate of reoxidation remained linear for between 1.5 and 3 minutes and with a high linear correlation as was shown in Figure 33. When the rate of reoxidation is plotted versus nitrite concentration, we see a linear trend as shown in Figure 34, with the slope being the second order rate constant.

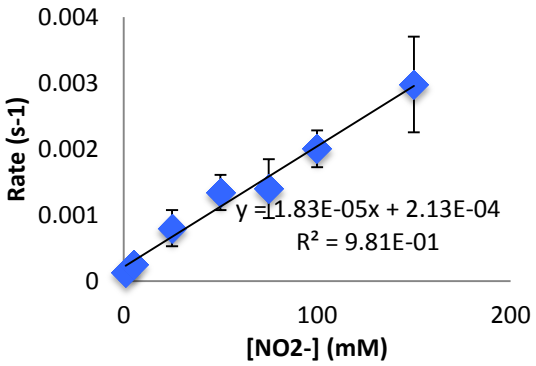

Figure – 34 Pseudo first order rates vs. [NO_2^-] for 100 µM NiR3His reduced by 1-2 equivalents of ascorbate.

Chapter 4: EPR Spectroscopy

4.1 Characterization of Variants Using EPR:

One of the ways that copper proteins can be characterized is by using electron paramagnetic resonance (EPR) spectroscopy. EPR spectroscopy can only be used to characterize our models in the oxidized form when the Type 1 and Type 2 copper sites are occupied by copper in the Cu(II) state. Cu(II) is a paramagnetic species with a $[Ar]3d^9$ electron configuration, meaning it has one unpaired electron. EPR uses a magnetic field to split the spin state levels for this unpaired electron into higher and lower energy levels as shown in Figure 35.[39] The splitting of the spin state levels is proportional to the magnitude of the magnetic field applied.[39] When a constant microwave frequency is applied to the sample, and the applied magnetic field is scanned over a range of intensities, unpaired electrons in the lower energy $m_s = – ½$ level will absorb the microwave energy and be transferred to the higher energy $m_s = + ½$ spin state.[39] This occurs when the microwave energy is equal to the energy difference between the spin state levels.[39] The energy of absorption is detected and used to create the EPR spectrum.

Not only does the applied magnetic field cause splitting of the electron spin state energies, so does the magnetic field that is generated by the spin of the copper nucleus. This causes hyperfine splitting, with the number of levels determined by the equation $2NI + 1$, where N is the number of nuclei present in the sample and I is the nuclear spin of the paramagnetic species.[39] These nuclear spin generated energy levels are referred to as m_I. For example, the Cu(II) atoms in our models have a nuclear spin of 3/2 giving rise to 4 hyperfine peaks.

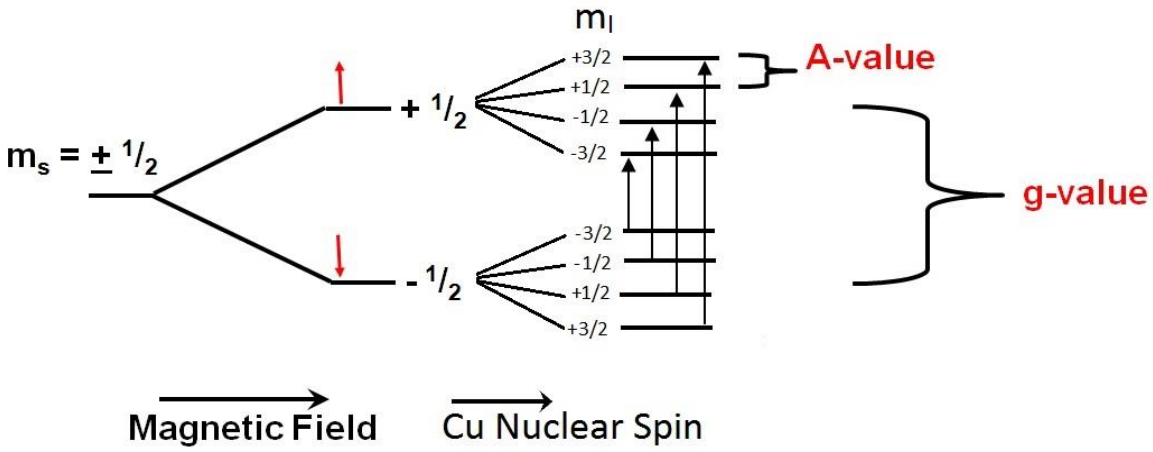

Figure – 35 representation of the splitting of the electron spin state orbital cause by an externally applied magnetic field as well as the magnetic field generated by the nuclear spin of the copper nucleus.

There are two values focused on in our Cu(II) EPR spectrum. These are the g-values, the splitting due to the external magnetic field, and the A-values, splitting due to the magnetic field generated by the copper nucleus. The g-value is further split into $g_{x,}$ g_y and $g_{z,}$ with each applying to a different axis of the copper-ligand bonds. Since the Type 1 and Type 2 copper sites on our model both typically exhibit axial symmetry, where the x and y-axis are equivalent, the g_x and g_y parameters are combined and referred to as $g_\perp$. The principal z-axis has a g-value referred to as $g_\parallel$. Similar to the g-values, A-values are dependent on the symmetry of the system, with axial systems having $A_\perp$ for A_x and A_y as well as $A_\parallel$ for A_z. Below in Figure 36 the $g_\parallel$ and $A_\parallel$-values are demonstrated on an axial copper EPR spectrum. The $g_\perp$ and $A_\perp$ in Figure 36 are located around a g-value of 2.0, but are difficult to determine without the aid of EPR simulation programs such as Simpow 6.

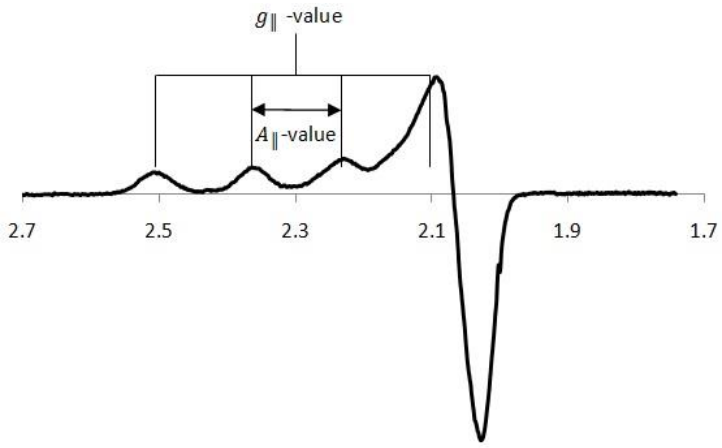

Figure 36 – Demonstration of the g-value and A-values parameters of an axial Cu(II) system such as the ones on our Type one and Type 2 copper centers.

Type 1 copper centers typically exhibit relatively small $A_{\parallel}$ values of < 80 gauss, as in the Type 1 copper of wild type azurin.[40] The cause of this small hyperfine splitting for Type 1 copper centers is derived from the high covalency of the Cu-S(Met) bond.[8,41,42] Type 2 coppers typically have $A_{\parallel}$ values of between 120-180 gauss.[40] In Figure 37 it is demonstrated how the Type 1 and Type 2 copper centers in our copper proteins can be measured separately. Additionally, since these copper sites are electronically independent of each other (they do not couple/interact), the resulting spectra are just an addition of each copper site.

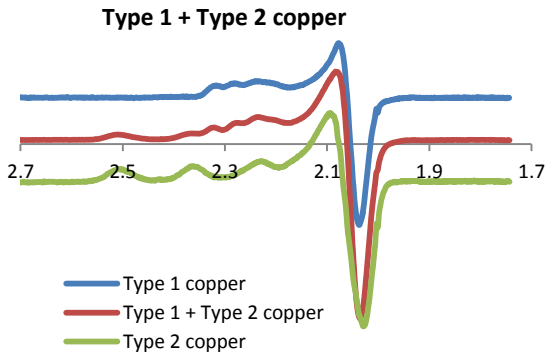

Figure 37 – Type 1 and Type 2 copper EPR spectrum individually as well as a Type 1 and Type 2 copper spectra demonstrating that the two individual copper spectrums can be added together to give the Type 1 plus Type 2 spectrum.

Both the parent as well as the "second generation" variants with single mutations of Phe15Trp, Phe114Pro and Met121Gln, had all been previously created and had characterized by EPR. After we created the double and triple mutants for each of the four parent variants, we begin characterizing them in order to compare them with our previous models. We took three different types of EPR spectra, one by binding copper to only the Type 1 site, another by binding copper to only the Type 2 site and a last spectrum by binding copper to both the Type 1 as well as the Type 2 site. The spectra for all of the variants are displayed in Figures 38-41 and the simulated $A_{\parallel}$ and $g_{\parallel}$ values listed in Tables 4-7.

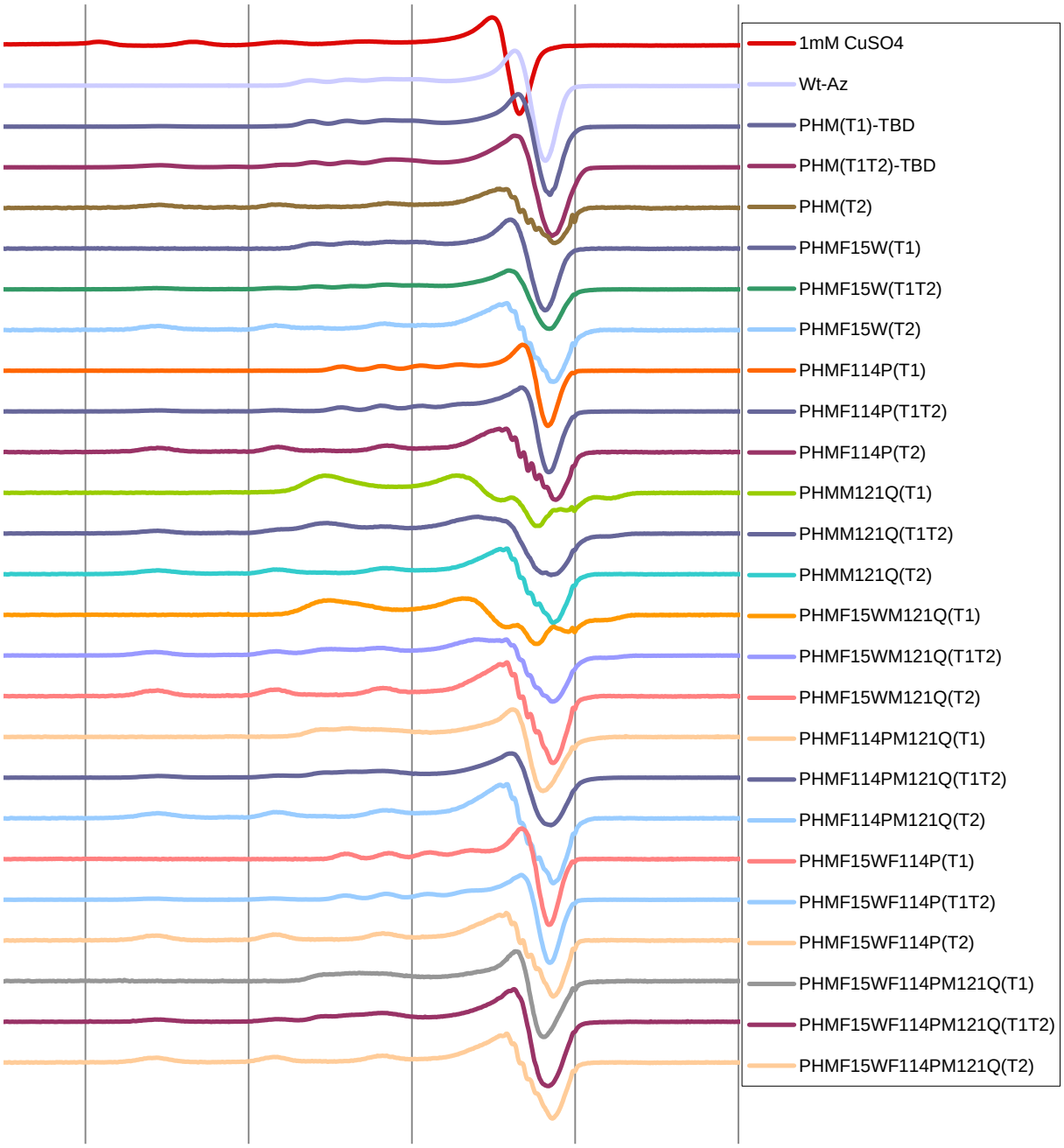

Figure 38 – Spectra of all of the PHM Variants

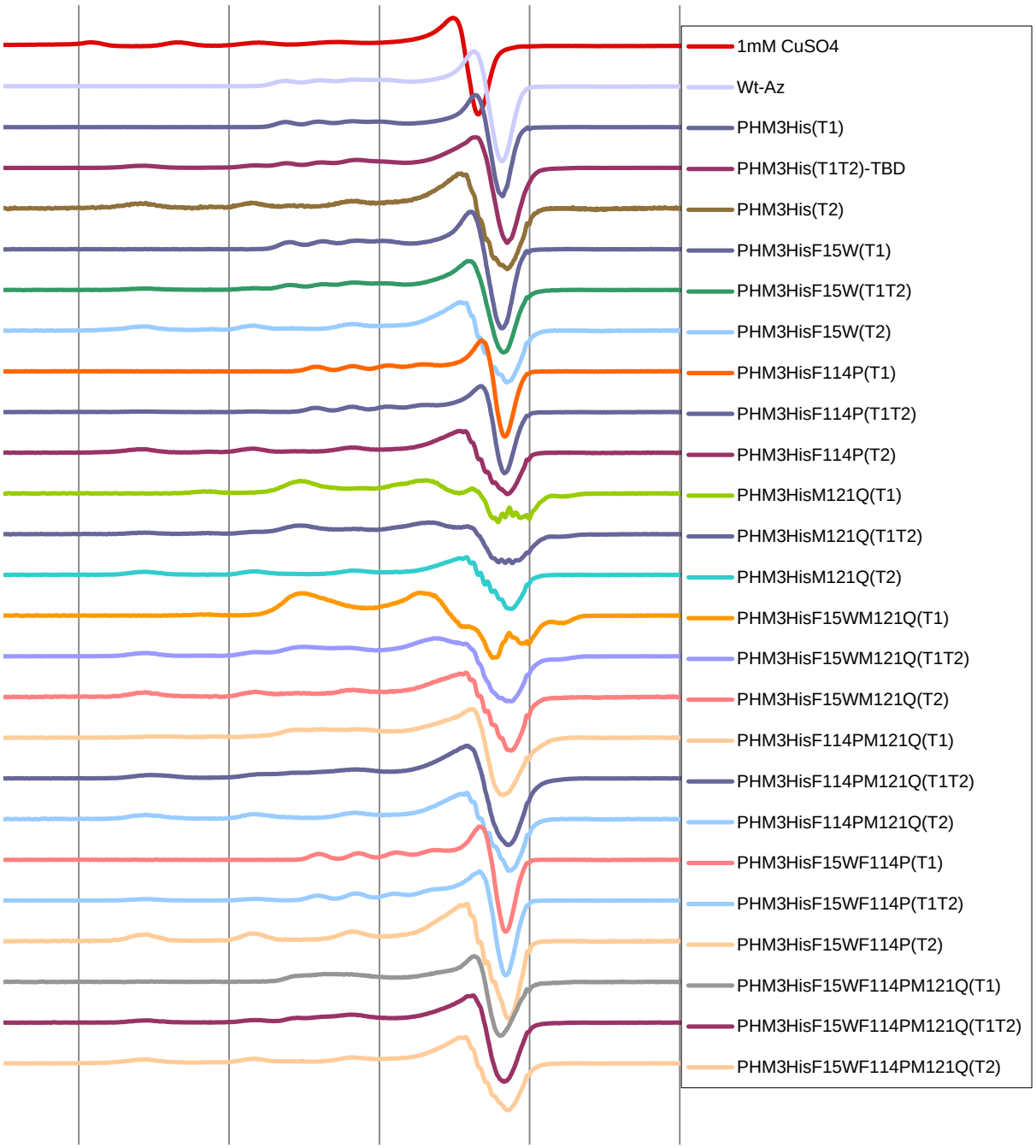

Figure 39 – Spectra of all of the PHM3His Variants

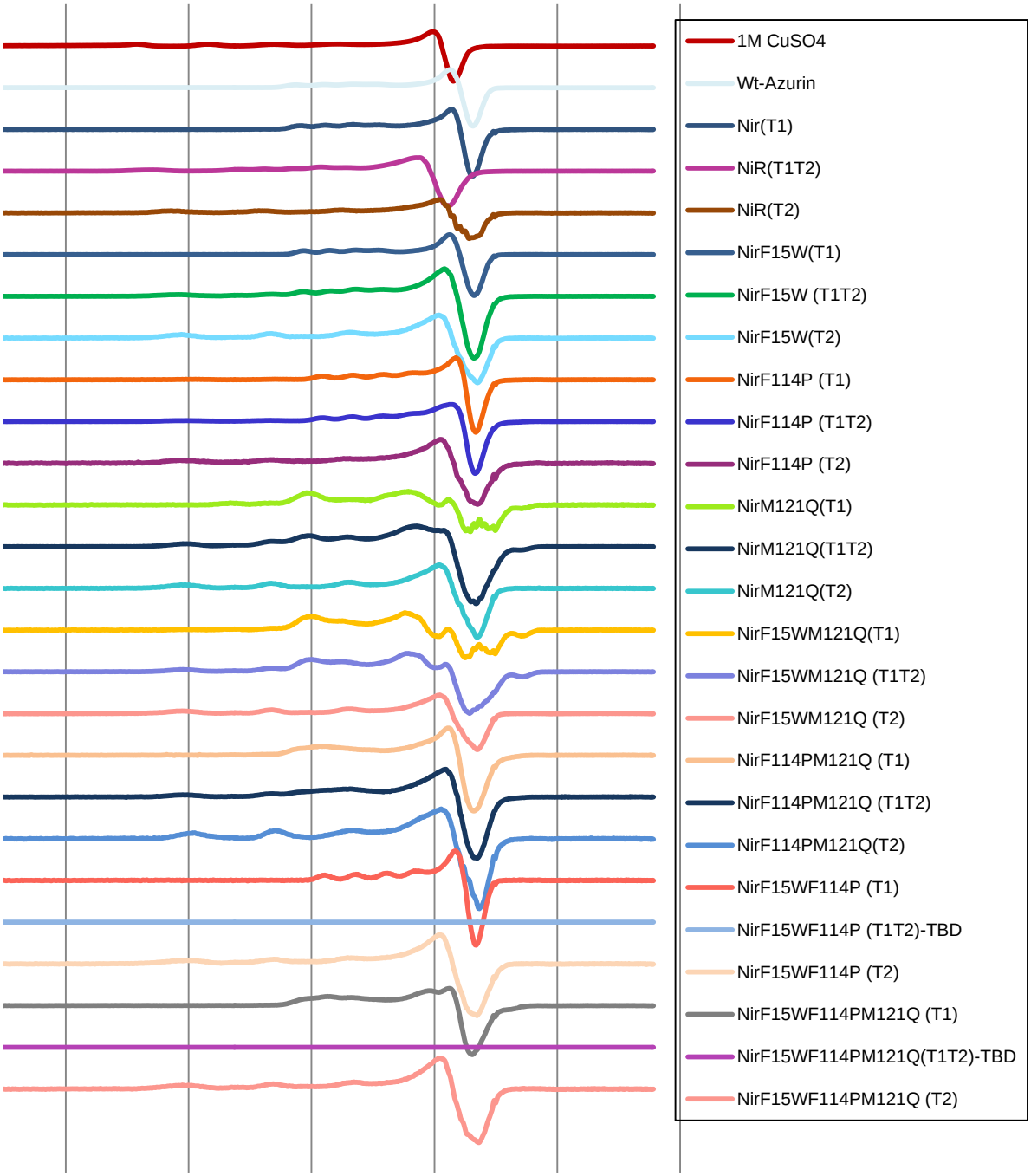

Figure 40 – Spectra of all of the NiR Variants

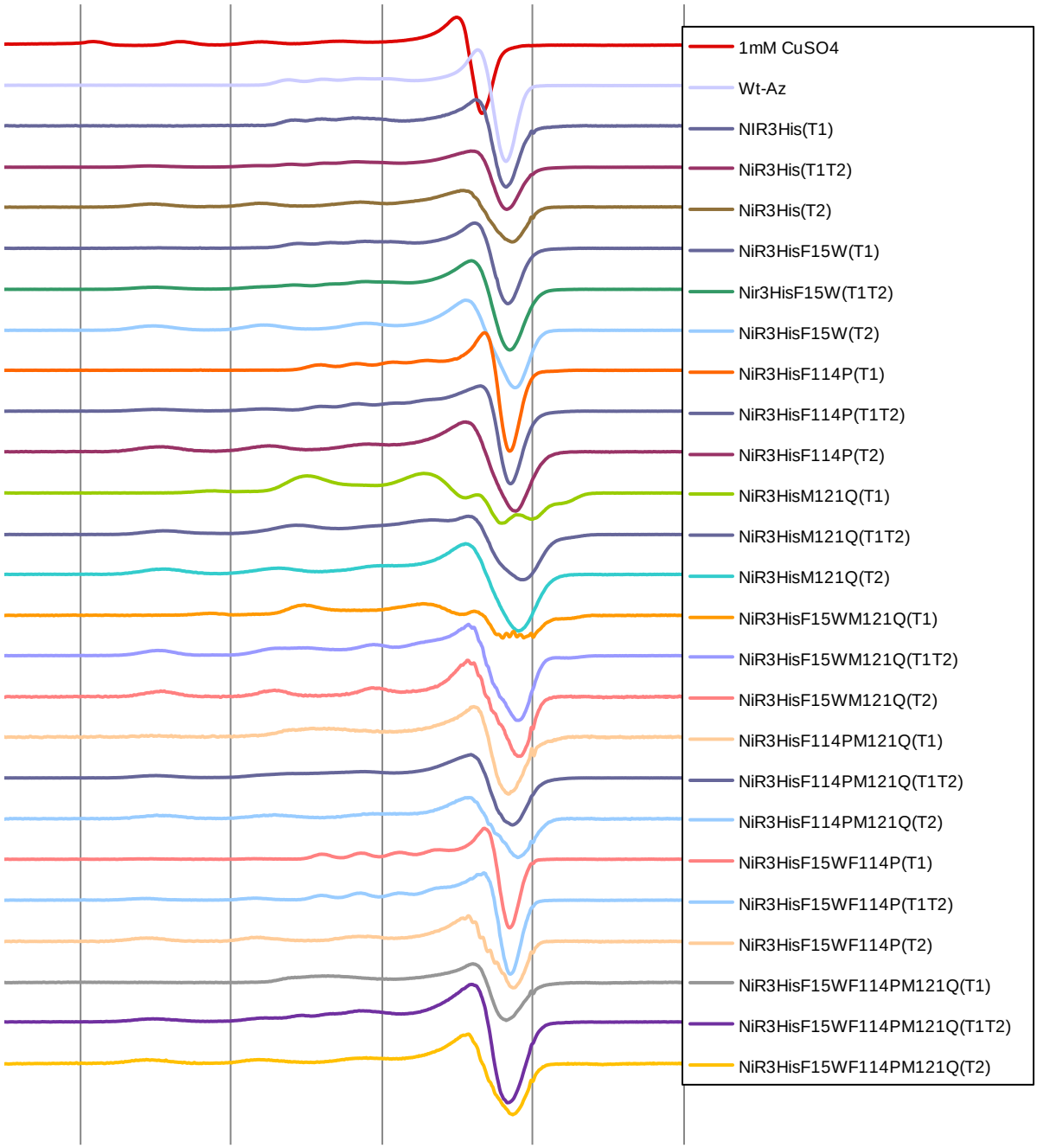

Figure 41 – Spectra of all of the NiR3His Variants

Table 4 - $g_{\parallel}$ values Type 1 copper (Gauss)

	Parent	F15W	F114P	M121Q	F15W F114P	F15W M121Q	F114P M121Q	F15W F114P M121Q
NiR3His	2.26	2.25	2.21	2.29	2.20	N/A	2.28	2.28
NiR	2.26	2.25	2.21	N/A	2.20	N/A	2.28	N/A
PHM3His	2.26	2.26	2.21	N/A	2.20	2.29	N/A	2.27
PHM	2.26	2.26	2.21	2.29	2.20	2.29	2.27	2.27
Native NiR from *A. x.* [43]	2.24							

Table 5 $g_{\parallel}$ values Type 2 copper (Gauss)

	Parent	F15W	F114P	M121Q	F15W F114P	F15W M121Q	F114P M121Q	F15W F114P M121Q
NiR3His	2.30	2.29	2.29	2.27	2.30	2.28	2.28	2.29
NiR	2.32	2.30	2.31	2.30	2.30	2.30	2.29	2.30
PHM3His	2.30	2.30	2.30	2.30	2.30	2.30	2.30	2.30
PHM	2.30	2.30	2.30	2.30	2.30	2.30	2.30	2.30
Native NiR from *A. x.* [43]	2.38							

Table 6 - $A_{\parallel}$ values Type 1 copper (Gauss)

	Parent	F15W	F114P	M121Q	F15W F114P	F15W M121Q	F114P M121Q	F15W F114P M121Q
NiR3His	47.14	53.45	61.90	N/A	68.02	N/A	37.77	36.20
NiR	52.43	51.53	64.95	N/A	66.22	N/A	33.92	N/A
PHM3His	53.09	53.41	62.54	N/A	68.02	17.56	N/A	36.51
PHM	53.23	52.83	63.46	20.76	67.27	20.08	39.29	36.51
Native NiR from *A. x.*[43]	63							

Table 7 - $A_{\parallel}$ values Type 2 copper (Gauss)

	Parent	F15W	F114P	M121Q	F15W F114P	F15W M121Q	F114P M121Q	F15W F114P M121Q
NiR3His	158.04	165.31	159.73	168.15	165.12	167.61	167.85	166.87
NiR	159.62	161.47	154.32	157.26	155.77	159.97	156.32	160.22
PHM3His	160.54	162.66	164.45	163.82	163.47	163.82	163.82	163.75
PHM	165.19	163.80	165.52	164.83	163.47	164.33	163.94	162.63
Native NiR from *A. x.*[43]	127							

As previously stated, for Type 1 copper centers an $A_{\parallel}$ of <80 gauss is expected. This is observed for all variants for which simulations have been successfully completed. The variants that include the Met121Gln mutation are often difficult to simulate for the Type 1 copper centers and some have yet to be fully refined. The difficulty arises from the Met121Gln mutation displaying a much more rhombic spectrum than the other variants. The rhombic spectrum is likely due to a shorter Cu-ligand bond distance for Cu-Gln than in Cu-Met as well as an increase of 0.2 Å of the copper out of the axial plane defined by the His_2Cys ligands.[44] This could induce rhombic splitting in the EPR spectrum by increasing the ligand field strength along the z-axis and increasing the amount of d_z^2 character of the HOMO.[8]

The Type 2 copper centers all display measured $A_{\parallel}$ and $g_{\parallel}$ values that are within the typical range, however there are a few slight differences between variants and between our models and the native NiR from *Alcaligenes xylosoxidans* (AxNiR). The Type 2 copper of AxNiR has a smaller $A_{\parallel}$ value than that of our models by about 35 gauss, indicating a higher degree of covalency of the AxNiR Type 2 copper with the histidine ligands.[43] Between our models, NiR3His, NiR and PHM3His all have $A_{\parallel}$ values of approximately 160 gauss, with a slight increase to 165 gauss for the PHM variant. The $g_{\parallel}$ values for all variants were approximately 2.3 gauss with little variation, this is slightly smaller than that of AxNiR, with a $g_{\parallel}$ value of 2.38 gauss.[43]

The results of the EPR measurements and simulations indicate that we have successfully maintained the Type 2 copper binding site for the single, double and triple variants. This validates the use of all of the variants as models to mimic the nitrite

reductase activity seen in native NiR's. Furthermore, the Type 1 copper site also remains intact but with varying amounts of perturbation that appear to be variant dependent, with the largest amount of perturbation of the Type 1 copper site coming from the incorporation of the Met121Gln mutation. These results are consistent with the UV-Visible absorption spectra for each variant as will be seen in chapter 5.

Chapter 5: UV-Visible Spectroscopy

5.1 Characterization of the Type 1 Copper Sites in the Azurin Model:

The parent variants were designed to add a second copper binding site on the surface of the protein approximately 12 Å from the Type 1 copper site to mimic the arrangement of copper in the noncoupled dinuclear copper protein family. These mutations are far enough away from the Type 1 center as to not affect the ligand binding environment around the copper. This can be seen when the UV-visible absorption spectra of the parent variants' Type 1 copper are overlaid with the spectrum for wild type azurin as seen in Figure 42.

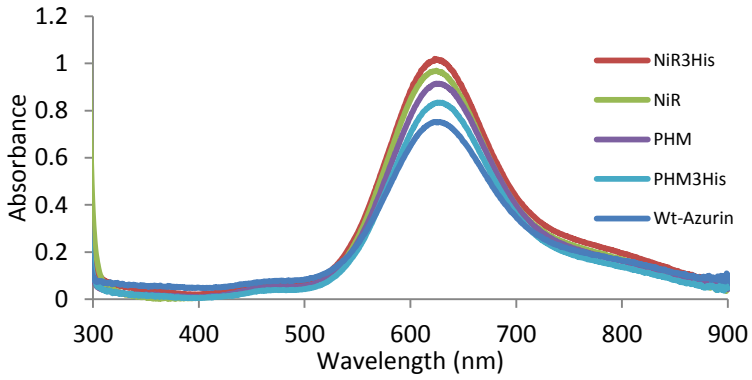

Figure 42 – The UV- Visible spectra of the four Parent variants and wild type azurin. Samples measured in 50 mM ammonium acetate buffer at pH 5.1.

The Phe15Trp mutation located between the Type 1 and Type 2 sites which was designed to aid in electron transfer between the two sites, and does not alter any of the ligands of both copper sites, results in little change to the UV-Visible spectra. Unlike the Phe15Trp mutation, the Phe114Pro and Met121Gln mutations are located in positions which either directly or indirectly affect the binding ligands of the Type 1 copper site.

The Phe114Pro mutation removes a hydrogen bond between Phe114 and Cys112 and is thought to allow Cys112 to move closer to the Type 1 copper.[7] Since the main absorption band is a S(Cys) $3p(\pi) \rightarrow$ Cu $3d_{x^2-y^2}$ LMCT, this results in the blue shifting of the main peak as well as increases in intensity of a shoulder around 800 nm due to a copper d→d transition. [6,8,45 ,46] Mutagenesis studies have shown that the Met121, His46 and His117 Type 1 copper ligands in azurin are not required for the characteristic blue color of the Type 1copper center, with the Cys112 ligand contributing the most to the color of the protein.[9] The Met121Gln mutation replaces the Type 1 methionine ligand with a glutamine, also blue shifting the spectra and greatly increasing the absorption of the S(Cys) $3p(\sigma) \rightarrow$ Cu $3d_{x^2-y^2}$ LMCT band that is observed around 450 nm.[8]

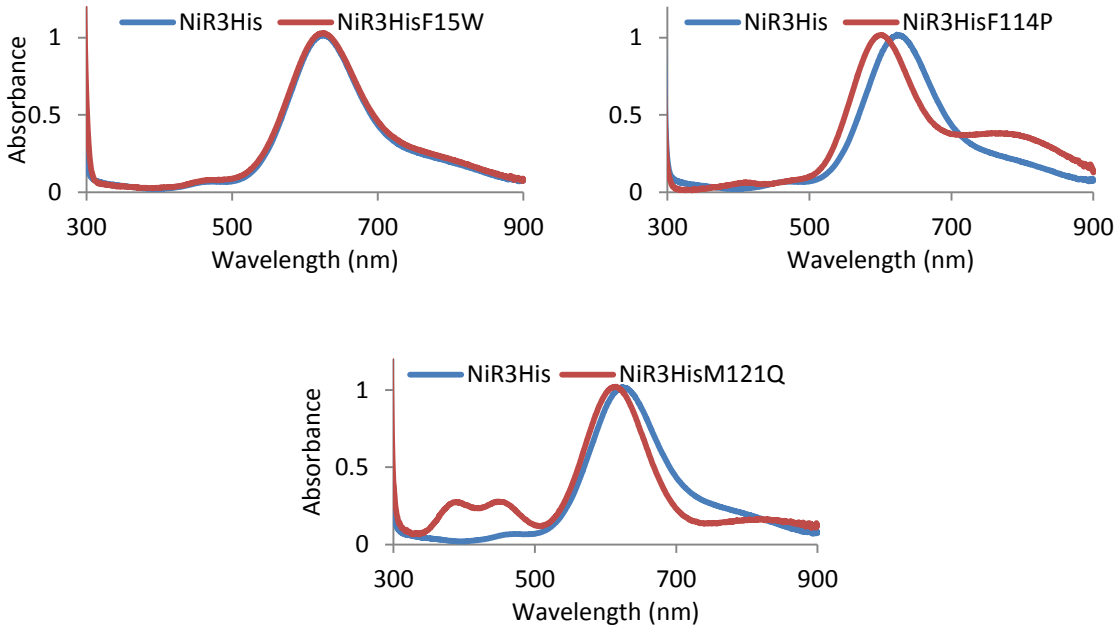

Figure 43 – Result that the F15W, F114P and M121Q mutations have on the UV- Visible spectra. Spectra were measured in 50 mM ammonium acetate buffer at pH 5.1.

When mutations are doubled and tripled up, the effects of each on the Type 1 copper signal is additive as seen with the variant NiR3His Phe15Trp Met121Gln. The variant NiR3His Phe15Trp has an absorption maxima at 625 nm, and the variant NiR3His Met121Gln has an absorption maxima at 611 nm. When these mutations are combined to create the NiR3His Phe15Trp Met121Gln variant, the absorption maxima is the average of the two, at 618 nm. Variants containing the Phe114Pro mutation tend to have an increase in the d→d transition observed near 800 nm and Met121Gln variants always show an increase in the S(Cys) $3p(\sigma) \rightarrow$ Cu $3d_{x^2-y^2}$band around 450 nm. Figures 44–51 show the Type 1 copper spectra for each variant arranged by parent.

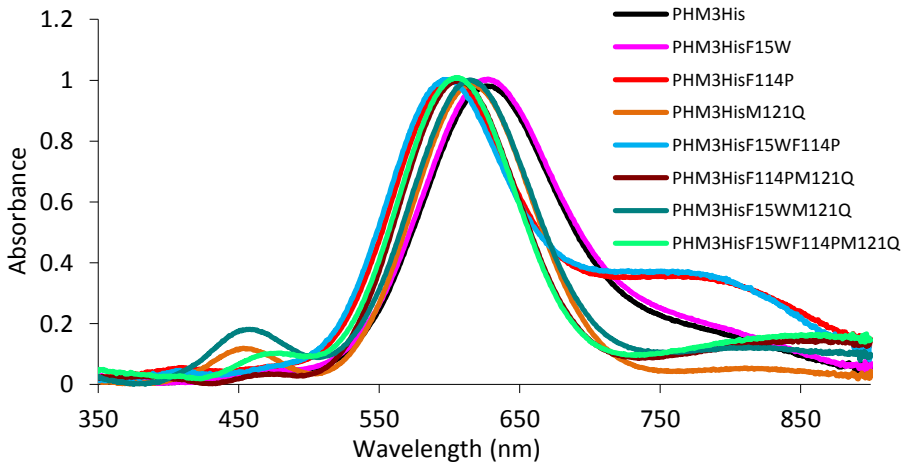

Figure 44 – UV-Visible of Type 1 copper site in PHM3His. Samples were in 50 mM ammonium acetate at pH 5.1.

Figure 44 shows an overlay of all variants of the parent PHM3His. Characteristic blue band at approximately 625 nm indicates the retention of the Type 1 copper site.

Bands at 450 nm for Met121Gln and 800 nm for Phe114Pro variants also appear and are maintained for the double and triple variants.

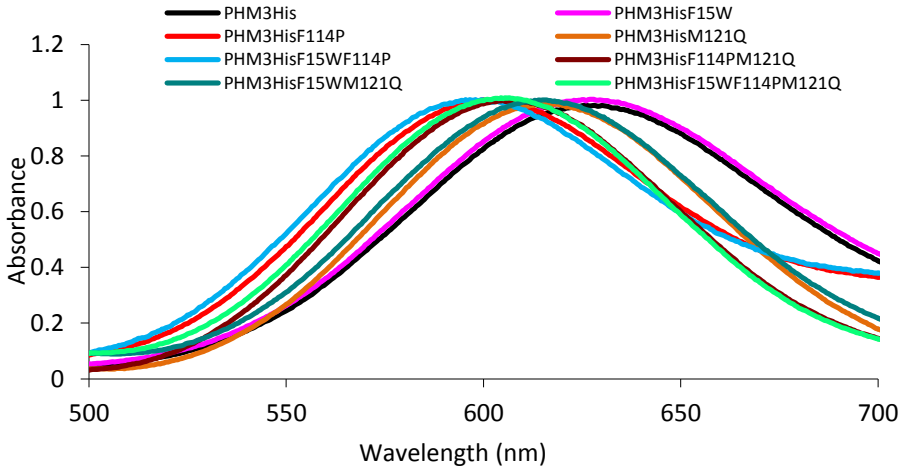

Figure 45 – Main UV- Visible peaks of PHM3His. Samples were in 50 mM ammonium acetate at pH 5.1.

Figure 45 shows a closer look at the absorption maxima for each variant of the parent PHM3His. The variants containing Met121Gln and Phe114Pro result in the largest deviations from the spectrum of the parent variant.

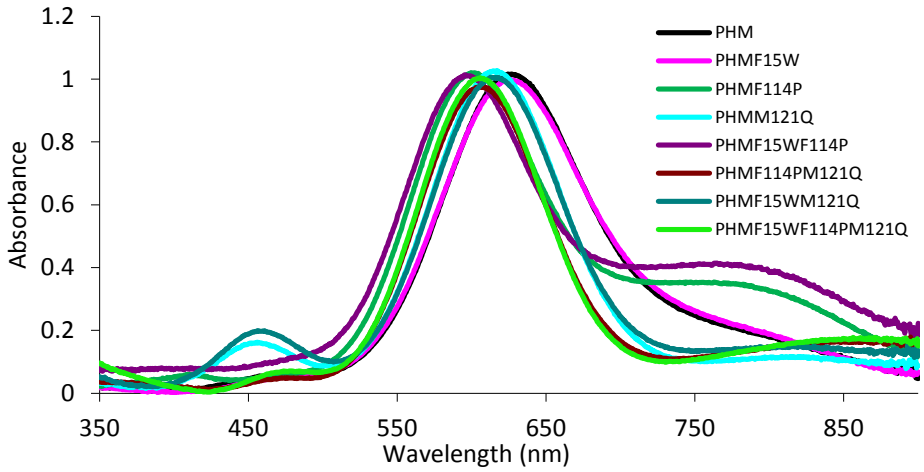

Figure 46 – UV- Visible of Type 1 copper site in PHM. Samples were in 50 mM ammonium acetate at pH 5.1.

Figure 46 shows the variants of the parent PHM. Again, variants containing the mutation Phe114Pro display an increase in the absorption band at 800 nm and variants containing the Met121Gln mutation have an increase in the absorption band at 450 nm.

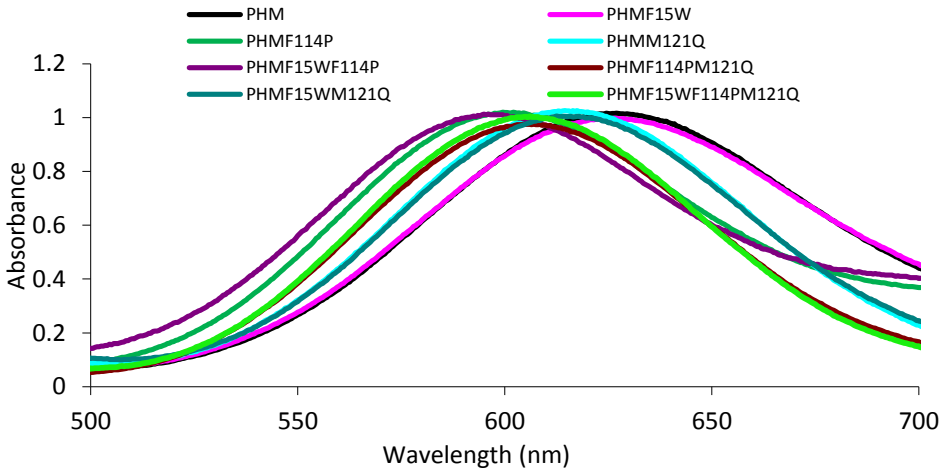

Figure 47 – Main UV- Visible peaks of PHM. Samples were in 50 mM ammonium acetate at pH 5.1.

Figure 47 shows a closer look at the main absorption band for the variants of the parent PHM. The trend of variants containing the mutations Met121Gln and Phe114Pro resulting in the largest deviation from the parent variant is still observed.

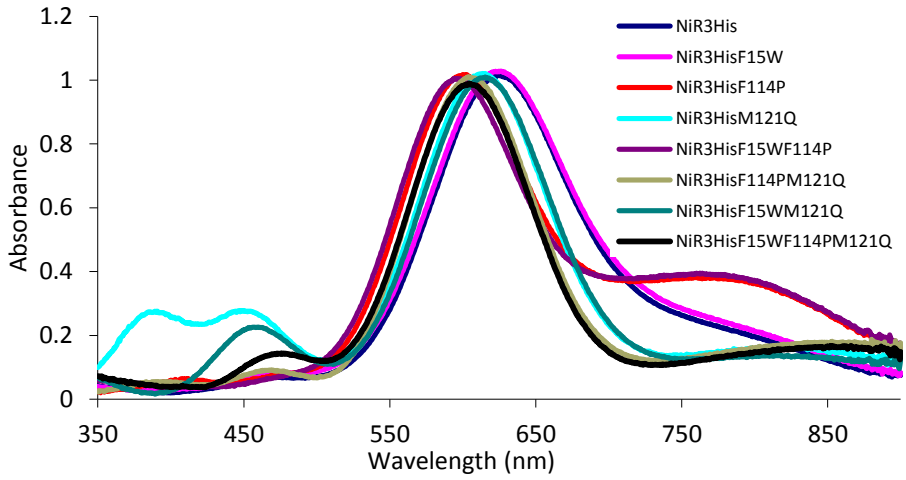

Figure 48 – UV- Visible of Type 1 copper site in NiR3His. Samples were in 50 mM ammonium acetate at pH 5.1.

In Figure 48 are the variants of the parent NiR3His. For the variant NiR3His Met121Gln a band appears at ~385 nm, which has previously been assigned to a S(Met) $b_1 \rightarrow$ Cu $3d_{x^2-y^2}$ transition for native NiRs.[8] However, the variant Met121Gln is the only variant displaying this band, so it is currently unclear exactly what this transition is due to since this variant lacks the methionine ligand.

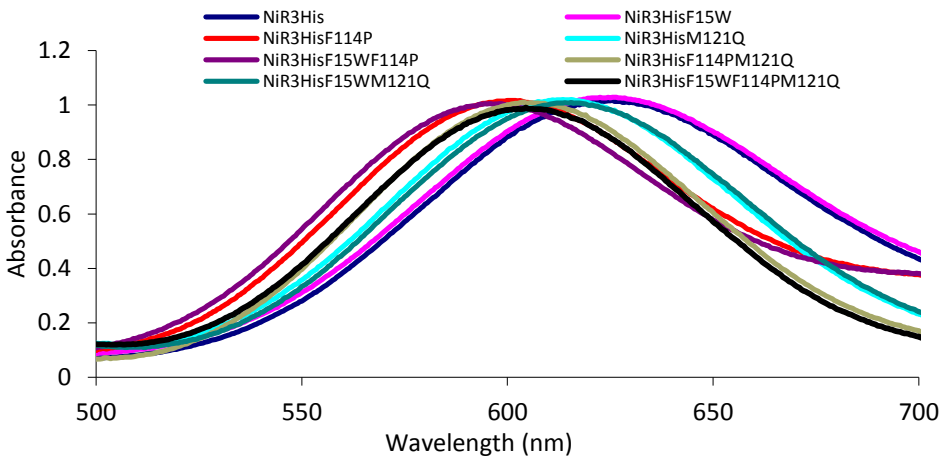

Figure 49 – Main UV- Visible peaks of NiR3His. Samples were in 50 mM ammonium acetate at pH 5.1.

The main blue absorption bands for the variants of NiR3His are shown in figure 49. Similar shifts in the absorption maxima are observed for the NiR3His variants when compared to the same mutations in the parent variants NiR, PHM and PHM3His.

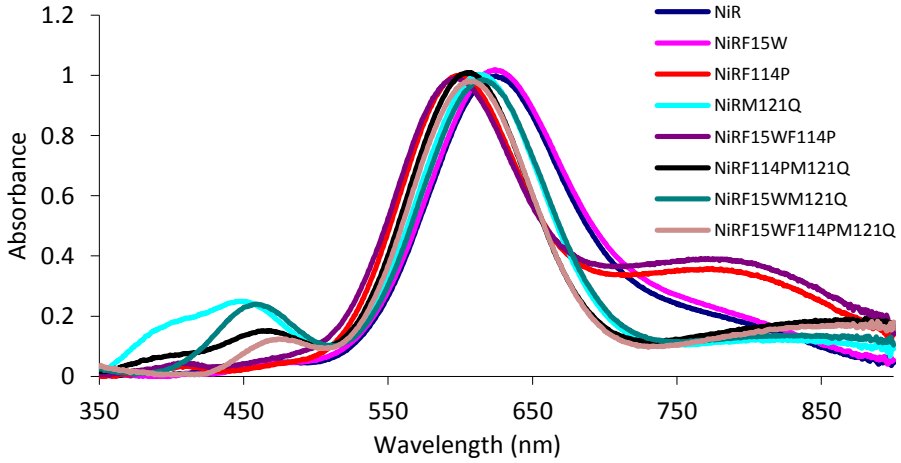

Figure 50 – UV- Visible of Type 1 copper site in NiR. Samples were in 50 mM ammonium acetate at pH 5.1.

An absorption band at ~385 nm is again observed for the variant NiRMet121Gln. This is similar to the spectra of the variant NiR3His Met121Gln.

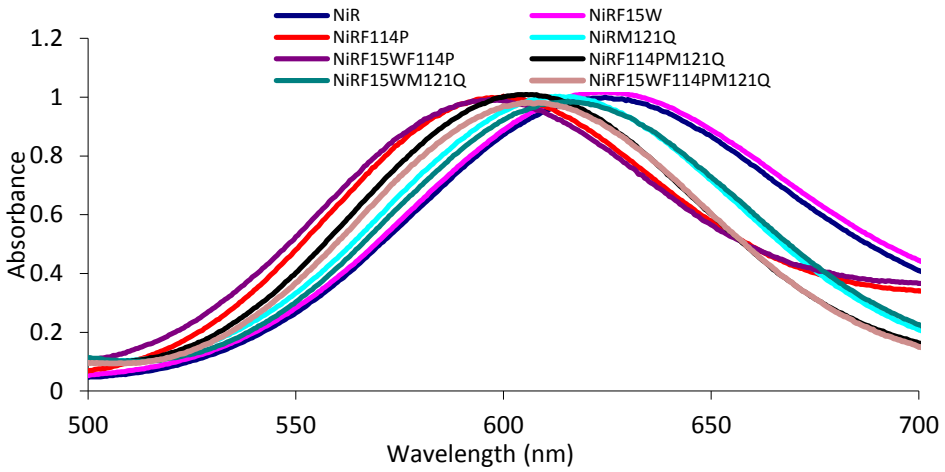

Figure 51 – Main UV- Visible peaks of NiR. Samples were in 50 mM ammonium acetate at pH 5.1.

These spectra demonstrate that the Type 1 copper site is conserved within all of the variants which were created. While there are some slight variations in the spectra as a result of differences in the geometry of the Type 1 copper site, this diversity of our models will allow us to more deeply explore what affects the kinetics of these variants.

5.2 Characterization of the Type 2 Copper Sites:

For all variants, UV-Vis spectra were taken of the Type 1copper bound protein that also contained a copper in the Type 2 site. However, since the Type 1 copper has an absorptivity of about 100 times that of the Type 2 sites, only the absorption peak due to

Type 1 centers can be observed. To obtain a spectrum for Type 2 copper centers, the Type 1 site must be populated with Hg(II) first before copper is added to the protein. Mercury has a higher binding affinity for the Type 1 site due to the presence of sulfur ligands found in methionine and cysteine.[13] The Type 2 center has no sulfur ligands, giving it a weak affinity for mercury and leaving it unoccupied for copper to bind. The Type 2 spectra have only been obtained for the parent variants so far and can be seen below in Figure 52.

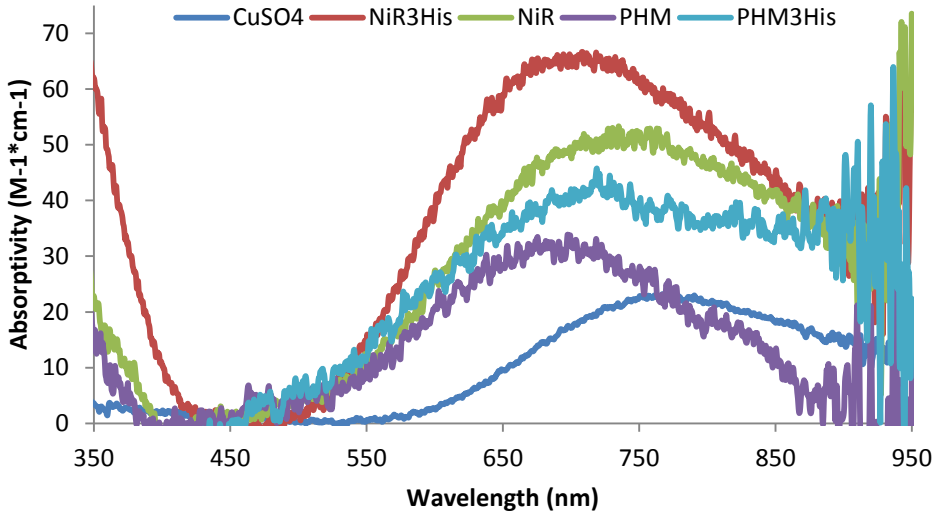

Figure 52 – Absorptivities of the parent Type 2 copper sites. Spectra taken in 50 mM ammonium acetate at a pH of 5.1.

The ε we observed for the Type 2 copper centers ranged from 31 $M^{-1}cm^{-1}$ for PHM up to 65 $M^{-1}cm^{-1}$ for our NiR3His model with absorbance maxes that ranged from 677-722 nm (Table 8). These values are comparable to the absorptivities and absorbance maximum that was observed for a de novo designed Type 2 copper center in 2012.[35] The absorbance of the Type 2 copper is attributed to Cu(II) *d-d* transitions.[35]

Table 8 – Absorptivities and maximum absorbance wavelengths of our parent variants as well as a de novo designed Type 2 copper site compared to $CuSO_4$ in solution.

	Absorptivity ($M^{-1}cm^{-1}$)	Absorbance Max (nm)
NiR3His	65	690
NiR	51	722
PHM3His	43	715
PHM	31	677
$CuSO_4$	24	764
Cu(II)(**TRI**L23H)$_3^{2+(8)}$	133-138	640

Conclusion and Future Directions:

Nitrogen is an important part of biological systems on Earth and it exists in many oxidation states ranging from -3 to +5. There are many enzymes involved in the conversion of nitrogen between these oxidation states. The work of this thesis was on modeling the copper containing nitrite reductases which take part in the reduction of nitrite to nitric oxide. By incorporation of a second copper binding site into the Type 1 copper electron transfer protein azurin, we were able to model the active site of these nitrite reductases.

Through the Griess assay and reoxidation assays we were able to show that our model enzymes follow Michaelis-Menten kinetics as well as determined the K_m and V_{max} values for our parent and second generation NiR3His variants. It was also shown that our model acts as a catalyst and produces NO as a product. While the turnover numbers of nitrite reduction achieved by our model are ~10^6 times slower than native systems, we still have a few models to test for their reactivity which may yield better results.

We also showed through EPR spectroscopy that our models have a second copper binding site, and that all but the Met121Gln retain the axial environment around the Type 1 copper site. The Met121Gln has a more rhombic environment due to the incorporation of a glutamate in the axial position. Additionally, we were able to characterize all of the Type 1 copper sites of our models using UV-Vis spectroscopy. Parent variants had little to no change in their spectra when compared to the wild type azurin, while variant containing mutations Phe114Pro and Met121Gln resulted in shifts of the main absorption band as well as increases in additional absorption bands. The F114P variants all resulted

in a blue shift of the main LMCT peak from 625 nm down to ~600 nm. There was also an increase in the Cu(II) d→d shoulder at 800 nm. M121Q seemed to have the largest effect on the protein, resulting in a change to a greenish blue color. This was due to a slight blue shift in the main LMCT peak as well as a large increase in the absorption bands around 400 nm which are due to the S(Cys) $3p(\sigma) \rightarrow$ Cu $3d_{x^2-y^2}$ transition.

The next steps will be to continue characterizing the remaining variants for their nitrite reductase activity. Also, we will seek to design additional variants with the intention of increasing the binding affinity of nitrite for the Type 2 catalytic center as well as increasing the V_{max}. Finally, we will attempt to also identify additional substrates toward which our model may have functional activity towards.

References:

1. Canfield, D. E.; Glazer, A. N.; Falkowski, P. G., *Science* **2010,** *330* (6001), 192-6.
2. Vitousek, P. M., Aber, J. D., Howarth, R. W., Likens, G. E., Matson, P. A., Schindler, D. W., Schlesinger, W. H., Tilman, D. G. , *Ecological Applications* **1997,** *7* (3), 737-50.
3. Wijma, H. J.; Canters, G. W.; de Vries, S.; Verbeet, M. P., *Biochemistry* **2004,** *43* (32), 10467-74.
4. Wilson, T. D.; Yu, Y.; Lu, Y., *Coord. Chem. Rev.* **2013,** *257* (1), 260-76.
5. Berry, S. M.; Ralle, M.; Low, D. W.; Blackburn, N. J.; Lu, Y., *J. Am. Chem. Soc.* **2003,** *125* (29), 8760-8.
6. Pinho, D.; Besson, S.; Brondino, C. D.; De Castro, B.; Moura, I., *Eur. J. Biochem.* **2004,** *271* (12), 2361-9.
7. Marshall, N. M.; Garner, D. K.; Wilson, T. D.; Gao, Y.-G.; Robinson, H.; Nilges, M. J.; Lu, Y., *Nature* **2009,** *462* (7269), 113-6.
8. LaCroix, L. B.; Shadle, S. E.; Wang, Y.; Averill, B. A.; Hedman, B.; Hodgson, K. O.; Solomon, E. I., *J. Am. Chem. Soc.* **1996,** *118* (33), 7755-68.
9. Mizoguchi, T. J.; Di Bilio, A. J.; Gray, H. B.; Richards, J. H., *J. Am. Chem. Soc.* **1992,** *114* (25), 10076-8.
10. Garner, D. K.; Vaughan, M. D.; Hwang, H. J.; Savelieff, M. G.; Berry, S. M.; Honek, J. F.; Lu, Y., *J. Am. Chem. Soc.* **2006,** *128* (49), 15608-17.
11. Li, H.; Webb, S. P.; Ivanic, J.; Jensen, J. H., *J. Am. Chem. Soc.* **2004,** *126* (25), 8010-9.
12. Leferink, N. G. H.; Han, C.; Antonyuk, S. V.; Heyes, D. J.; Rigby, S. E. J.; Hough, M. A.; Eady, R. R.; Scrutton, N. S.; Hasnain, S. S., *Biochemistry* **2011,** *50* (19), 4121-31.
13. Holm, R. H.; Kennepohl, P.; Solomon, E. I., *Chem. Rev.* **1996,** *96* (7), 2239-314.
14. Abraham, Z. H. L.; Smith, B. E.; Howes, B. D.; Lowe, D. J.; Eady, R. R., *Biochem. J.* **1997,** *324* (2), 511-6.
15. Murphy, M. E. P.; Turley, S.; Adman, E. T., *J. Biol. Chem.* **1997,** *272* (45), 28455-60.

16. Adman, E.; Watenpaugh, K. D.; Jensen, L. H., *Proc. Natl. Acad. Sci. U.S.A.* **1975,** *72* (12), 4854-8.
17. Strange, R. W.; Murphy, L. M.; Dodd, F. E.; Abraham, Z. H. L.; Eady, R. R.; Smith, B. E.; Hasnain, S. S., *J. Mol. Biol.* **1999,** *287* (5), 1001-9.
18. Wijma, H. J.; Jeuken, L. J. C.; Verbeet, M. P.; Armstrong, F. A.; Canters, G. W., *J. Biol. Chem.* **2006,** *281* (24), 16340-6.
19. Lee, W., Tolman, W. B., *Inorg. Chem.* **2002,** *41* (22), 5656-8.
20. Chang, T. K.; Iverson, S. A.; Rodrigues, C. G.; Kiser, C. N.; Lew, A. Y. C.; Germanas, J. P.; Richards, J. H., *Proc. Natl. Acad. Sci. U.S.A.* **1991,** *88* (4), 1325-9.
21. Husain, M.; Davidson, V. L., *J. Biol. Chem.* **1985,** *260* (27), 14626-9.
22. Harris, R. L.; Eady, R. R.; Hasnain, S. S.; Sawers, R. G., *Arch. Microbiol.* **2006,** *186* (3), 241-9.
23. Dodd, F. E.; Hasnain, S. S.; Hunter, W. N.; Abraham, Z. H. L.; Debenham, M.; Kanzler, H.; Eldridge, M.; Eady, R. R.; Ambler, R. P.; Smith, B. E., *Biochemistry* **1995,** *34* (32), 10180-6.
24. Wijma, H. J.; MacPherson, I.; Alexandre, M.; Diederix, R. E. M.; Canters, G. W.; Murphy, M. E. P.; Verbeet, M. P., *J. Mol. Biol.* **2006,** *358* (4), 1081-93.
25. Pozdnyakova, I.; Guidry, J.; Wittung-Stafshede, P., *Biophys. J.* **2002,** *82* (5), 2645-51.
26. Rizzuti, B.; Daggett, V.; Guzzi, R.; Sportelli, L., *Biochemistry* **2004,** *43* (49), 15604-9.
27. Yamada, T.; Hiraoka, Y.; Ikehata, M.; Kimbara, K.; Avner, B. S.; Das Gupta, T. K.; Chakrabarty, A. M., *Proc. Natl. Acad. Sci. U.S.A.* **2004,** *101* (14), 4770-5.
28. Yang, D.-S.; Miao, X.-D.; Ye, Z.-M.; Feng, J.; Xu, R.-Z.; Huang, X.; Ge, F.-F., *Pharmacol Res* **2005,** *52* (5), 413-21.
29. Berry, S. M.; Gieselman, M. D.; Nilges, M. J.; Van der Donk, W. A.; Lu, Y., *J. Am. Chem. Soc.* **2002,** *124* (10), 2084-5.
30. Suzuki, S.; Kataoka, K.; Yamaguchi, K., *Acc. Chem. Res.* **2000,** *33* (10), 728-35.
31. Berry, S. M.; Mayers, J. R.; Zehm, N. A., *J. Biol. Inorg. Chem.* **2009,** *14* (1), 143-9.

32. Shih, C.; Museth, A. K.; Abrahamsson, M.; Blanco-Rodriguez, A. M.; Di Bilio, A. J.; Sudhamsu, J.; Crane, B. R.; Ronayne, K. L.; Towrie, M.; Vlcek, A., Jr.; Richards, J. H.; Winkler, J. R.; Gray, H. B., *Science* **2008,** *320* (5884), 1760-2.
33. Moody, A. J.; Shaw, F. L., *Anal. Biochem.* **2006,** *356* (1), 154-6.
34. Steiner, A. A.; Van Winden, H., *Plant Physiol.* **1970,** *46* (6), 862-3.
35. Tegoni, M.; Yu, F.; Bersellini, M.; Penner-Hahn, J. E.; Pecoraro, V. L., *Proc. Natl. Acad. Sci. U.S.A.* **2012,** *109* (52), 21234-9, S/1-S/10.
36. Miranda, K. M.; Espey, M. G.; Wink, D. A., *Nitric Oxide* **2001,** *5* (1), 62-71.
37. Giustarini, D.; Rossi, R.; Milzani, A.; Dalle-Donne, I., *Methods Enzymol.* **2008,** *440* (Nitric Oxide, Part F), 361-80.
38. Voet, D., Voet, J. G., *Biochemistry*. 4th ed.; John Wiley & Sons, INC.: 2011; p 1428.
39. Parish, R. V., *NMR, NQR, EPR, and Mössbauer Spectroscopy in Inorganic Chemistry*. Ellis Horwood Ltd: 2003; p 223.
40. McCleverty, J. A., Meyer, Thomas J., *Comprehensive Coordination Chemistry II: From Biology to Nanotechnology*. 2nd ed.; Elsevier Science: 2003; Vol. 8.
41. Shadle, S. E.; Penner-Hahn, J. E.; Schugar, H. J.; Hedman, B.; Hodgson, K. O.; Solomon, E. I., *J. Am. Chem. Soc.* **1993,** *115* (2), 767-76.
42. Penfield, K. W.; Gewirth, A. A.; Solomon, E. I., *J. Am. Chem. Soc.* **1985,** *107* (15), 4519-29.
43. Prudencio, M.; Eady, R. R.; Sawers, G., *J. Bacteriol.* **1999,** *181* (8), 2323-9.
44. Romero, A.; Hoitink, C. W. G.; Nar, H.; Huber, R.; Messerschmidt, A.; Canters, G. W., *J. Mol. Biol.* **1993,** *229* (4), 1007-21.
45. Gewirth, A. A.; Solomon, E. I., *J. Am. Chem. Soc.* **1988,** *110* (12), 3811-9.
46. Hadt, R. G.; Sun, N.; Marshall, N. M.; Hodgson, K. O.; Hedman, B.; Lu, Y.; Solomon, E. I., *J. Am. Chem. Soc.* **2012,** *134* (40), 16701-16.